Investigation of using limestone calcined clay cement (LC3) in engineered cementitious composites: The effect of propylene fibers and the curing

JOURNAL OF MATERIALS RESEARCH AND TECHNOLOGY 2021;15:2117–2144

Available online at www.sciencedirect.com

jmr&t Journal of Materials Research and Technology

journal homepage: www.elsevier.com/locate/jmrt

Original Article

Investigation of using limestone calcined clay cement (LC3) in engineered cementitious composites: The effect of propylene fibers and the curing system

Jun Liu [a], *Weizhuo Zhang* [a], *Zhenlin Li* [a], *Hesong Jin* [a,*], *Wei Liu* [a], *Luping Tang* [b]

[a] *Guangdong Provincial Key Laboratory of Durability for Marine Civil Engineering, College of Civil and Transportation Engineering, Shenzhen University, Shenzhen, 518060, PR China*

[b] *Department of Architecture and Civil Engineering, Division of Building Technology, Chalmers University of Technology, 41296, Gothenburg, Sweden*

ARTICLE INFO

Article history:
Received 3 July 2021
Accepted 6 September 2021
Available online 9 September 2021

Keywords:
Engineered cementitious composites (ECCs)
Limestone calcined clay cement (LC3)
PP fibers
Improved compressive constitutive model
Microstructures
Pore size and porosity

ABSTRACT

Limestone calcined clay cement (LC3) is a new type of low-carbon cement that can reduce energy consumption and carbon dioxide emissions while meeting the performance requirements of ordinary cement. In this study, polypropylene (PP) fibers were mixed into limestone calcined clay cement-based materials to make new low-carbon ECCs. In this study, a total of 24 sets of specimens were designed for 4 groups of curing ages and 6 types of mix ratios. The compressive load–displacement data were measured the compressive curve characteristics were analyzed then, a compressive constitutive model of the composites was deduced and obtained. Through XRD, SEM-EDS and MIP experiments, the reasons and laws of the compressive strength ranges of adding PP fibers and LC3 to engineered cementitious composites (LC3-PP-ECCs) are further explained from the perspective of the pore size, microstructures and hydration products. The results show that, after 28 days, the compressive strength values of LC3-PP-ECCs generally decreases with increasing PP fiber content and the combined effect of PP fibers and hydration products causes the compressive strength of LC3-ECCs with 0.5% PP fibers to drop sharply. In addition, the specimens showed better properties in terms of toughness, ductility and energy absorption. However, in the microstructures, the addition of PP fibers will cause more internal defects and flaws. This results of this study can provide some theoretical experience and technical support for the engineering application of LC3-ECCs.

* Corresponding author.
E-mail address: hesongjin@szu.edu.cn (H. Jin).

https://doi.org/10.1016/j.jmrt.2021.09.023

1. Introduction

Cement is an indispensable and important material and it has been used in construction and infrastructure construction for a long time. In the 1990s, Victor C. Li et al. began to try to mix fibers into cement and established a theoretical model of the pull-out test that considers the change in the bond strength during the pull-out process [1]. Composite materials composed of fiber and cement have begun to be widely studied. At present, fiber-reinforced cement-based composite materials have been studied on with a variety of fibers, including steel fibers [2,3], polyethylene fibers [4,5], polypropylene fibers [6], glass fibers [7,8] and plant fibers [9,10]. There are differences in the properties of the different types of fibers. To obtain cement-based composites with better comprehensive performance, some current studies investigated [11,12] mixed multiple fibers.

Engineered cementitious composites (ECCs) are advanced fiber-reinforced cement-based composite materials with excellent tensile strain capacity and strain hardening performance [13,14]. According to the theory of micromechanics, the synergy between the fibers, matrix and fibers/matrix are combined in ECCs. The ECCs will not lose their load-bearing capacity immediately after the first crack. The tensile strain capacity of typical ECCs is greater than 3% [15]. The strain hardening capacity of ECCs can reach hundreds of times that of traditional concrete [16]. In addition, the crack width of ECCs can be controlled to below 100 μm even under extreme compression, bending and tensile loads and large deformations [15–17]. Therefore, the abovementioned excellent features of ECCs help to improve the elasticity, durability and sustainability of cement-based materials [18–20], prevent cement-based materials from cracking due to their brittleness and improve the safety of RC structures. Their excellent mechanical properties make ECCs widely used building materials [21]. However, most ECCs will not only increase the cost of material production but also the raw materials that require a large amount of cement and polymer fibers will generate large energy and carbon footprints [22,23].

Baiano et al. emphasized the need of environment-friendly, alternative and, ideally, carbon-neutral strategies for energy production [24]. Fossil fuel consumption is responsible for CO_2 emissions and adverse global environmental changes. Portland cement is always regarded as the main contributor to the environmental impact and energy consumption of cementitious materials [25]. Because its production needs to consume a lot of fossil fuels. The cement industry is one of the largest producers of carbon dioxide (CO_2), accounting for approximately 7% of total atmospheric CO_2 emissions [26,27]. The use of auxiliary cementitious materials (SCMs) to reduce cement will become the developing trend of green building materials. Because materials such as fly ash (FA) and metakaolin are different from ordinary Portland cement (OPC), they not only do not consume energy during the production process but also do not produce carbon dioxide [6,28]. In the study of SCMs, it was found that using an SCM can reduce the energy consumption by 71% when compared to benchmark materials [29]. The energy consumption of LC3 cement-based composites was also lower than that of ordinary concrete [30]. Thus its use is very advantageous. In this context, various SCMs have been extensively studied. Hosan and Shaikh combined nano-$CaCO_3$ with high-volume slag and slag-fly ash concrete. They found that its carbon footprint was reduced by 54% and its 28 d compressive strength was greater than that of the control OPC concrete [31]. Chun et al. found that the tensile strength of a strain hardening superfast hardening mortar containing a large amount of an auxiliary cementing material and polyethylene fiber can reach 7.3 MPa [4]. Zeyad et al. studied high-strength concrete mixed with volcanic pumice powder and polypropylene fiber. They found that it can replace cement for production and it would reduce costs [6]. Souza et al. used limestone powder instead of OPC for the production of prefabricated slender structural mortar components. They found that its strength is higher than 40 MPa and that it has good durability [32].

Using supplementary cementitious materials (SCMs) to replace part of the cement can be a reliable solution that can not only reduce energy consumption and greenhouse gas emissions but also avoid binder quality problems [33,34]. Some studies [35–38] have explored the effect of commonly used SCMs on the performance and durability of concrete, confirming the feasibility of using SCMs. On this basis, the use of SCMs such as fly ash, slag, pozzolan and silica fume have also been extensively studied in ECCs [39–44] and they have also shown good performance. However, most of these SCMs are industrial byproducts and the existing reserves and predicted output will not be able to meet the expected demand for cement [45–47]. Therefore, these SCMs are difficult to use on a large scale. In contrast, calcined clay will have greater advantages in the future because clay minerals are naturally present in the Earth crust throughout the world [48] and calcined clay can be produced by only heat treatment. The progressive reduction of fossil resources and the severe environmental problems associated with their extensive use are pushing both academia and industry to resort to different routes for the development of more sustainable added-value products and processes. The progressive reduction of fossil resources and their widespread use have brought serious environmental problems. It has prompted academia and industry to resort different routes for the development of more sustainable added-value products and processes [49]. The advantage of limestone over cement is that it does not need to consume fossil resources for calcination. At the same time, the replacement of limestone in OPC mixtures with calcined

Table 1 – The main chemical composition of raw materials (%).

Type of materials	SiO_2	Al_2O_3	CaO	K_2O	Fe_2O_3	MgO	SO_3
Calcined clay	55.8	38	0.26	3.35	1.57	0.35	0.18
Cement	20.31	5.62	61.78	1.55	3.54	2.11	2.47

(a) Appearance of raw materials

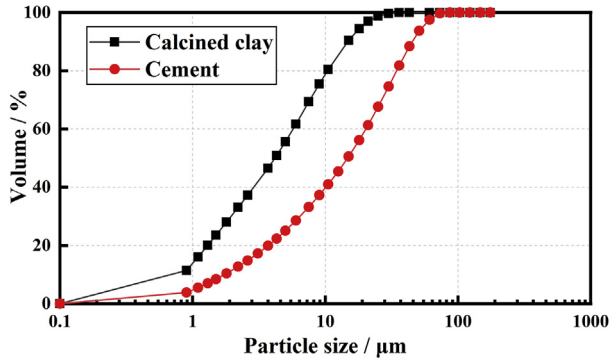

(b) Particle size distribution

Fig. 1 – Raw materials (cement, limestone powder, calcined clay powder, gypsum powder and PP fiber).

clay shows ideal compressive strength and durability by producing aluminates that promote the formation of ettringite [50–53]. Combining calcined clay and limestone has become an outstanding solution [54]. This method shows a higher level of clinker replacement and at a high replacement rate, it can maintain the same or even exceed the mechanical properties [46,55,56], durability [57] and physical and chemical properties of OPC [58–61]. In addition, it has been demonstrated that LC3 cement can be mass-produced in existing factories [62,63]. A large number of studies has shown that LC3 has the characteristics of low carbon, environmental protection, economy and good performance, which means that LC3-ECCs have great research value.

At present, there have been preliminary evaluations of LC3-ECCs and the 28 day compressive strength values of LC3-ECCs meets the requirements of RC structures [64]. At the same time, LC3-ECCs are more malleable, more durable, more environmentally friendly and has a less expensive than OPC-ECCs [30], which means that LC3 has shown feasibility in developing low-carbon ECCs with good tensile ductility. In previous studies [30,64–66], a 2% volume content of fibers was selected for study. As a new material, it is necessary to consider the effect of fiber contents on LC3-ECCs. In addition, there have been only a few studies on the compressive performance of LC3-ECCs and the reasons for the ranges in compressive performance have not been studied enough and explained in consideration of multiple factors.

Based on the above research background, starting from the excellent performance of LC3-ECCs, this study explores the compressive performance and law of LC3-PP-ECCs under 4 different curing ages and 6 different fiber contents. Among these conditions, he cross-section and failure states of the specimens were observed. Through XRD, SEM-EDS and MIP, the crystal compositions, micromorphology and compound products of the LC3-ECCs were explored and the toughening mechanism of the PP fibers was explained. At the same time, the mechanical properties of LC3-PP-ECCs, such as compressive stress and strain, were studied and a summary of the law of changes in the mechanical properties of LC3-ECCs under the combined effects of the various fiber contents and curing ages were evaluated. At the same time, the mechanical properties of LC3-PP-ECCs, such as stress and strain, were studied and the range law of the mechanical properties of LC3-ECCs was summarized under the combined effects of the various PP fiber contents and curing ages. Based on this, the feasibility and applicability of LC3-ECCs were investigated and the results of this investigation provide some ideas and experience for accelerating the promotion and application of new low-carbon ECCs.

2. Experimental design and raw materials

2.1. Raw materials

Fig. 1(a) shows the raw materials, including P·O 42.5 ordinary Portland cement (OPC), limestone powder, calcined clay powder, gypsum powder and polypropylene fiber and their particle size distributions are shown in Fig. 1(b). This study selected Conch brand commodity ordinary Portland cement produced in Yingde City, Guangdong Province, which complies with *GB 175–2007 General Portland Cement* [67]. Table 1 shows the chemical composition of the raw material. For the PP fibers, the length of the PP fiber was 1.2 cm, the diameter was 25 μm, the Young's modulus was 7.1 GPa and the tensile strength was 630 MPa. The detailed description of the project was also published elsewhere [68].

2.2. Design of mix ratio and preparation of test pieces

The mix ratio of this study refers to previous studies [57,69]. The water-to-binder ratio (w/b) usually ranges from 0.35 to 0.5. A w/c of 0.4 was selected in this study. In the amounts of

Table 2 – Mixture proportions of LC3-ECCs (kg/m^3).

Mixtures NO.	W/B	Binder proportion				PP fibers
		OPC	CC	LS	GYP	
LC3-PP-1	534.22	702.93	400.67	200.33	31.63	0.00
LC3-PP-2	531.55	699.41	398.66	199.33	31.47	4.55
LC3-PP-3	528.88	695.89	396.66	198.33	31.32	9.10
LC3-PP-4	526.20	692.37	394.65	197.33	31.16	13.65
LC3-PP-5	523.53	688.85	392.65	196.32	31.00	18.20
LC3-PP-6	520.86	685.34	390.64	195.32	30.84	22.75

Note: LC3 in mixture NO. is for limestone calcined clay cement, PP is for PP fibers, and the numbers 1, 2, 3, 4, 5 and 6 in mixture NO. are 0%, 0.5%, 1%, 1.5%, 2% and 2.5% of PP fibers blended in volume, respectively. OPC: ordinary Portland cement; CC: calcined clay; LS: limestone; GYP: gypsum.

cementitious materials, OPC accounts for 50%, calcined clay powder accounts for 30%, limestone powder accounts for 15% and gypsum powder accounts for 5%. The OPC used therein contains 5% gypsum, and only 2.4% gypsum is added when calculating and weighing. This study employed 4 different curing ages, namely, 1 d, 3 d, 7 d and 28 d. In addition, 6 different PP fiber contents were designed and the volume ratios were 0%, 0.5%, 1%, 1.5%, 2% and 2.5% with 3 specimens in each group. The specific volumes of raw materials are shown in Table 2.

The production process is shown in Fig. 2 and the preparation of mortar refers to *GB/T 17671–1999 "Cement Mortar Strength Inspection Method (ISO Method)"* [70]. According to the designed raw material ratios, the amounts of each material were carefully weighed. Then, the cementitious materials were placed into the mixtures and stirred for 2 min so that the cementitious materials were evenly mixed. Then, the PP fibers were evenly added around the sides into the mixer and water was slowly added after the PP fibers were completely added. The speed of the mixer was adjusted and the mixer was operated slowly and quickly for 2 min. After the mixing was completed, the PP fibers that remained on the equipment were put into the container. The fully stirred mixtures were placed into a mold of 40 mm × 40 mm × 160 mm and placed on a vibrating table. At the same time, the pastes were filled three times. The calcined clay in LC3 is very viscous and the incorporation of PP fibers will also introduce air bubbles. Then, the outer surface of the finished specimen was wrapped with plastic wrap to ensure that moisture was not lost, and the hydration reaction of the test pieces proceeded normally. After 24 h of setting, the test specimens had a certain mechanical strength and the model was removed and the specimen was placed in a standard curing room with a temperature of 20 ± 2 °C and a relative humidity of 95%.

2.3. *Compressive test*

The compressive strength was tested by a constant-load cement flexural and compressive testing machine, as shown in Fig. 3(a). The equipment adopted displacement control and the loading rate was 1 mm/min. The test refers to *GB/T 17671–1999 "Cement Mortar Strength Test Method (ISO Method)"* [70] and to the literature [71]. Through processing, the compressive stress–strain curves of the materials can be obtained. Based on the literature [71], the compressive characteristics of the peak stress σ_m, peak strain ε_m, elastic modulus **E**, residual stress σ_u and residual strain ε_u in the curve characteristics can be obtained. The analysis methods of these parameters are described in detail in Chapter 3.2.2. By further analysis, it can be obtained the compressive constitutive model of the ECCs.

2.4. *XRD test*

To analyze the specimen product phases, this study applied an X-ray diffractometer (the model is MICROXCT-400, manufactured by XRADIA Company, America), as shown in Fig. 3(b). The scanning angle was set to the 2θ range of 5–80° and the phase composition ranges of the samples were collected [72]. The specimens were analyzed after the destruction of the compression test. The sample was placed in a drying oven to dry and then it was ground to below 5 μm. The sample powder was compacted on a glass dish and placed in the instrument for measurement.

2.5. *SEM-EDS test*

To study the microscopic structures of the pastes, this study applied scanning electron microscopy-energy dispersive

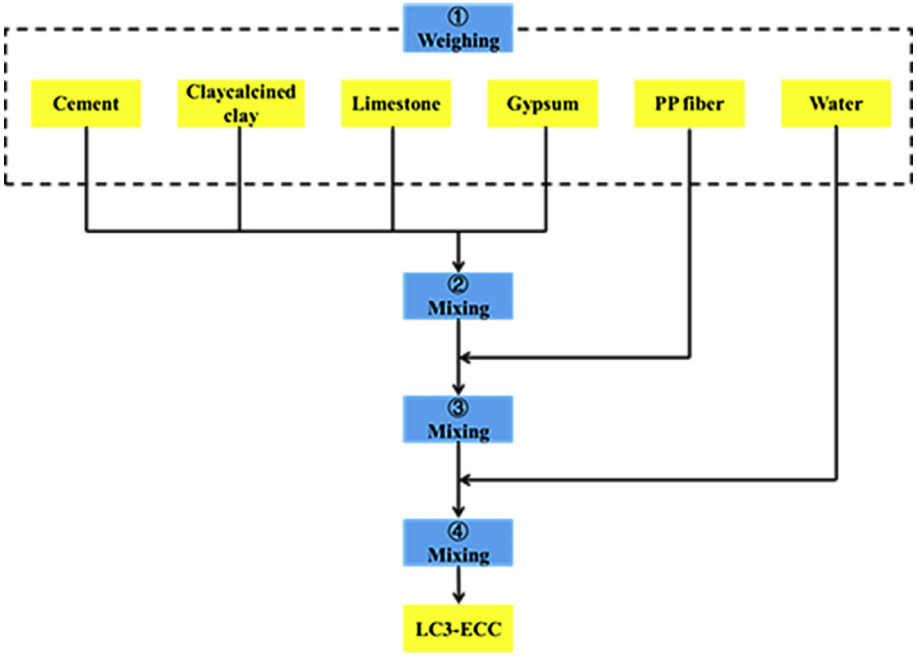

Fig. 2 – Production process of the LC3-PP-ECCs specimens.

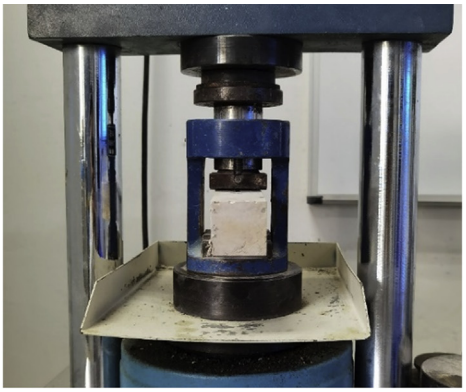

(a) Compressive equipment

(b) XRD equipment

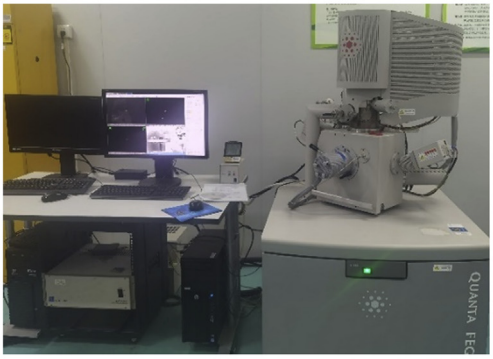

(c) SEM-EDS equipment

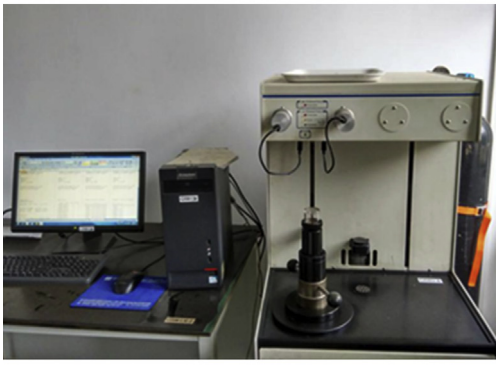

(d) MIP equipment

Fig. 3 – Test equipment.

spectrum analysis (Quanta TM 250 FEG, manufactured by FEI Company, America), as shown in Fig. 3(c). The broken specimens from the compression test were placed in a drying box for drying. In this study, pieces of the paste of approximately 5 mm from the surface and internal area of the mixtures were extracted. . Moreover, to increase the electrical conductivity of SEM specimens, the samples were gold plating before the test [73].

2.6. *MIP test*

To analyze the pore size and porosity of ECC mixtures, this study applied mercury intrusion porosimetry (MIP) and the mercury intrusion instrument (Autopore IV 9500 porosimeter, Micromeritics, USA), which is often selected to study the pores of mixtures, as shown in Fig. 3(d). The samples used in this study were taken from the surface of the ECC pastes, the diameter of the samples was approximately 5–15 mm and the samples were placed in an oven at 30–60 °C for 24 h before the MIP analyses [72].

3. Results and discussion

3.1. *Patterns of compressive failure*

Fig. 4 (a)-(f) show compression failure characteristics of the six groups of specimens LC3-PP-1, LC3-PP-2, LC3-PP-3, LC3-PP-4, LC3-PP-5 and LC3-PP-6 after curing for 28 days. Because LC3-PP-1 was not added PP fiber, during the process of compressive failure the parts at both ends will break first and then the internal cracks will spread out from the outer edge. When the cracks penetrate, they will peel off layer by layer, as shown in Fig. 4 (a), and the final shape of the specimens will be similar to a pit. For LC3-PP-2, LC3-PP-3, LC3-PP-4, LC3-PP-5 and LC3-PP-6-containing PP fibers, it can be observed from Fig. 4 that, due to the connection and bridging effect of the PP fibers, the specimens will not be completely separated when they are broken, and the cracks will basically expand vertically. In addition, transverse cracks can be observed in the specimens with low PP fiber volumes. However, for specimens with large amounts of PP fibers, the above phenomenon will not appear. Moreover, the numbers of cracks are relatively small, the compressive failure time is longer and the specimens are more intact after compressive damage.

Fig. 5 shows the compressive fracture section of the ECC test pieces. After comparison and observation, it can be found that there are some pores and bubbles on the cross-section. Among them, bubbles with larger diameters are more likely to appear in LC3-PP-1, indicating that the addition of PP fibers can be combined with LC3, preventing the existence of larger diameter bubbles. With the increase in the PP fiber volume, the number of pores with a diameter lower than 1 mm on the cross-section also increases, indicating that the incorporation of PP fibers will cause small bubbles in the ECC matrix, which negatively affects the mechanical properties of LC3-ECCs. In addition, the distribution of PP fibers can also be observed on the cross section. Due to its excessive fiber content of 2.5% by volume, the fiber distribution on the cross-section of LC3-PP-6 is obviously uneven and there are agglomerations of PP fibers

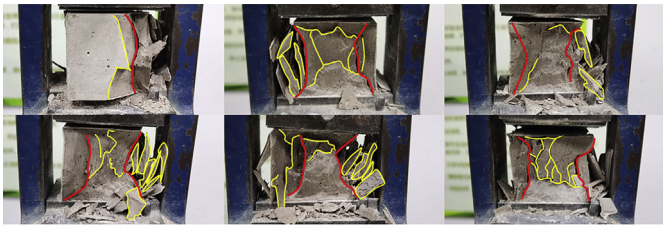

(a) Compressive failure form of LC3-PP-1

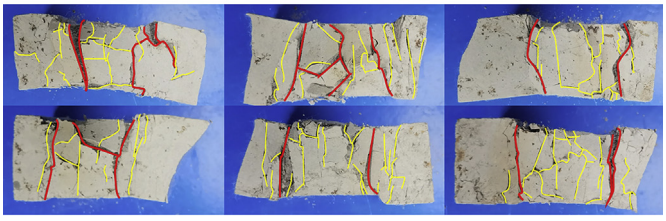

(b) Compressive failure form of LC3-PP-2

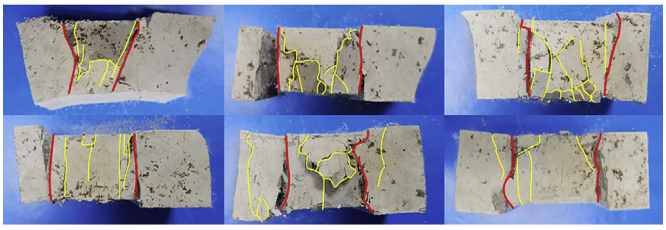

(c) Compressive failure form of LC3-PP-3

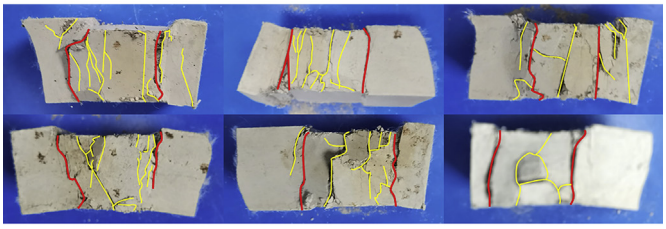

(d) Compressive failure form of LC3-PP-4

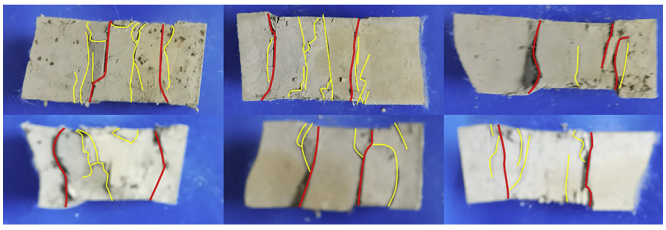

(e) Compressive failure form of LC3-PP-5

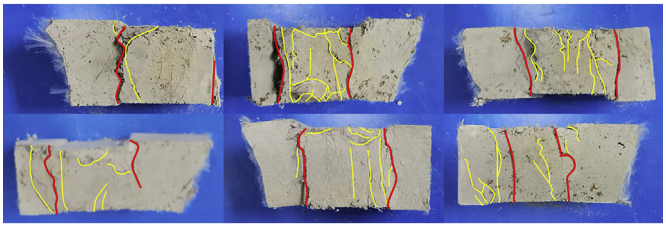

(f) Compressive failure form of LC3-PP-6

Fig. 4 – Different compressive failure patterns of the ECCs after 28 days curing age.

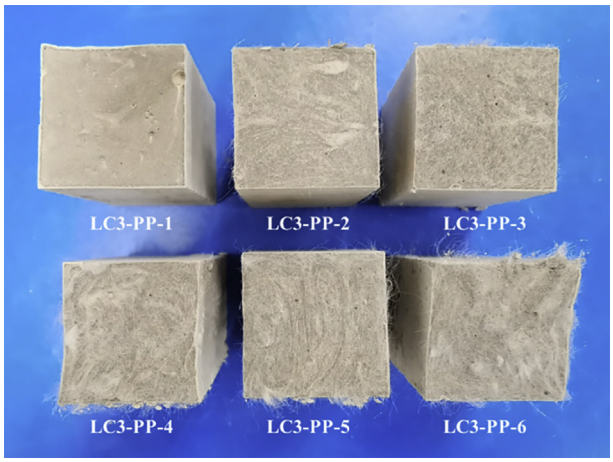

Fig. 5 – Compressive fracture cross-section of the LC3-ECCs.

in some areas, which will have an impact on the mechanical properties of LC3-ECCs.

3.2. σ-ε curves analysis of LC3-PP-ECCs

3.2.1. Overall analysis of compressive σ-ε curves

Fig. 6 (a)–(f) show the σ-ε curves of specimens LC3-PP-1, LC3-PP-2, LC3-PP-3, LC3-PP-4, LC3-PP-5 and LC3-PP-6 at 4 curing ages. Through the analysis, the influence of the curing ages on the compressive performance of LC3-ECCs can be explored. Fig. 6 shows that the σ-ε curves of the LC3-PP-ECCs are similar to those of other ECCs and the curves are mainly composed of a linear rising stage and a nonlinear descending stage. Fig. 6 shows that in the initial compressive phase, the line segment basically grows in a straight line and, as it approaches the peak, the slope gradually decreases. Through comparison, it can be found that, at early curing ages, the shapes of the σ-ε curve at the peak are smoother and with longer curing ages the shapes of the σ-ε curves ages are sharper. At the same time, with the longer the curing age of the specimens, the faster the curve in the descending process. In the subsequent stages, the σ-ε curves gradually flattened out, until they finally tend to extend horizontally. For the same group of specimens with different curing ages, the heights of the linear stage are very similar.

Fig. 7 explores the influence of the fiber volume on the compressive performance of LC3-ECCs, where Fig. 7 (a), (b), (c) and (d) correspond to curing ages of 1 d, 3 d, 7 d and 28 d, respectively. Fig. 7 shows that with increasing PP fiber volume, there is no significant difference in the peak strain of each group of LC3-ECC specimens. The peak stress gradually decreases and LC3-PP-1 is obviously the maximum in each group after 3 d, 7 d and 28 d of curing ages. After 1 d, the slope of each group of specimens in the ascending phase is relatively discrete and the slope of LC3-PP-1 is the largest. At 3 d, 7 d and 28 d, the slopes of the curves of each group become closer and it can be observed that the slopes of the 6 groups of specimens are basically the same after 28 d; the curves in the rising phase are basically coincident. This shows that, under a curing age of 28 days, the PP fiber content has little effect on the elastic modulus. At the peak, the specimens with more PP fiber content formed a smoother arc, while the specimens with less PP fiber content formed a sharper arc. In the descending stage, the curves of the specimens with lower PP fiber content decreases faster, so the curves can be observed to intersect in Fig. 7. This causes the curves to change from the highest peak stress to the smallest stress, and the other groups also change the order of height in turn. In the next stage, the σ-ε curves begin to extend horizontally.

3.2.2. Overall phase analysis of the σ-ε curves

By analyzing the σ-ε curves (shown in Figs. 6 and 7), it can be found that there is a certain change law between the compressive stress and strain of the LC3-ECCs. Through further analysis, the σ-ε curve is made (shown in Fig. 8(a)). The development of the curve is divided into multiple stages and the stress characteristics of each stage are described separately, combined with experimental phenomena, and the effects of changes in different curing ages and fiber contents are explained.

(1). **OA** stage

The OA stage is the linear growth phase. In this stage, the LC3-ECCs undergo elastic deformation under uniaxial compressive loading, the appearance of ECCs does not change significantly and the initial internal defects basically do not expand. As long as the loading process does not exceed this stage, the mechanical properties and appearance dimensions of the specimens can be restored to their original state. The slope of this stage is the elastic modulus **E**, which can be used to measure the ability to resist elastic deformation. The elastic modulus is affected by factors such as the fiber content and curing age. Point A is the upper limit of the elastic phase. When this limit is exceeded, the slope of the curve begins to change and more cracks begin to occur after point A.

(2). **AB** stage

At the beginning of the AB stage, the slope changes from the original linear growth to nonlinear growth. This stage is no longer an elastic stage so, when the ECCs reach this stage, the deformation produced is only partially reversible. The slope of the first half has a small change. The initial internal defects and shrinkage microcracks have just begun to extend and the cracks were in a stable expansion state. Careful observation can reveal the spread of microcracks. The slope changes obviously in the second half and the stress inside the specimens increases slowly during the loading displacement of the equipment. At this time, it can be clearly observed that the cracks continue to extend and the crack width becomes larger. If loading continues, for the LC3-PP-1 specimens without PP fibers, after the main cracks penetrate, the surface of the specimens begins to peel off for the first time. This phenomenon occurs when point B is approaching and the whole process is very fast. For the other five groups of specimens with added PP fibers, the fracture noise of the PP fibers due to compression or drawing can be clearly heard. Different from the LC3-PP-1 group without fiber, due to the bonding effect of

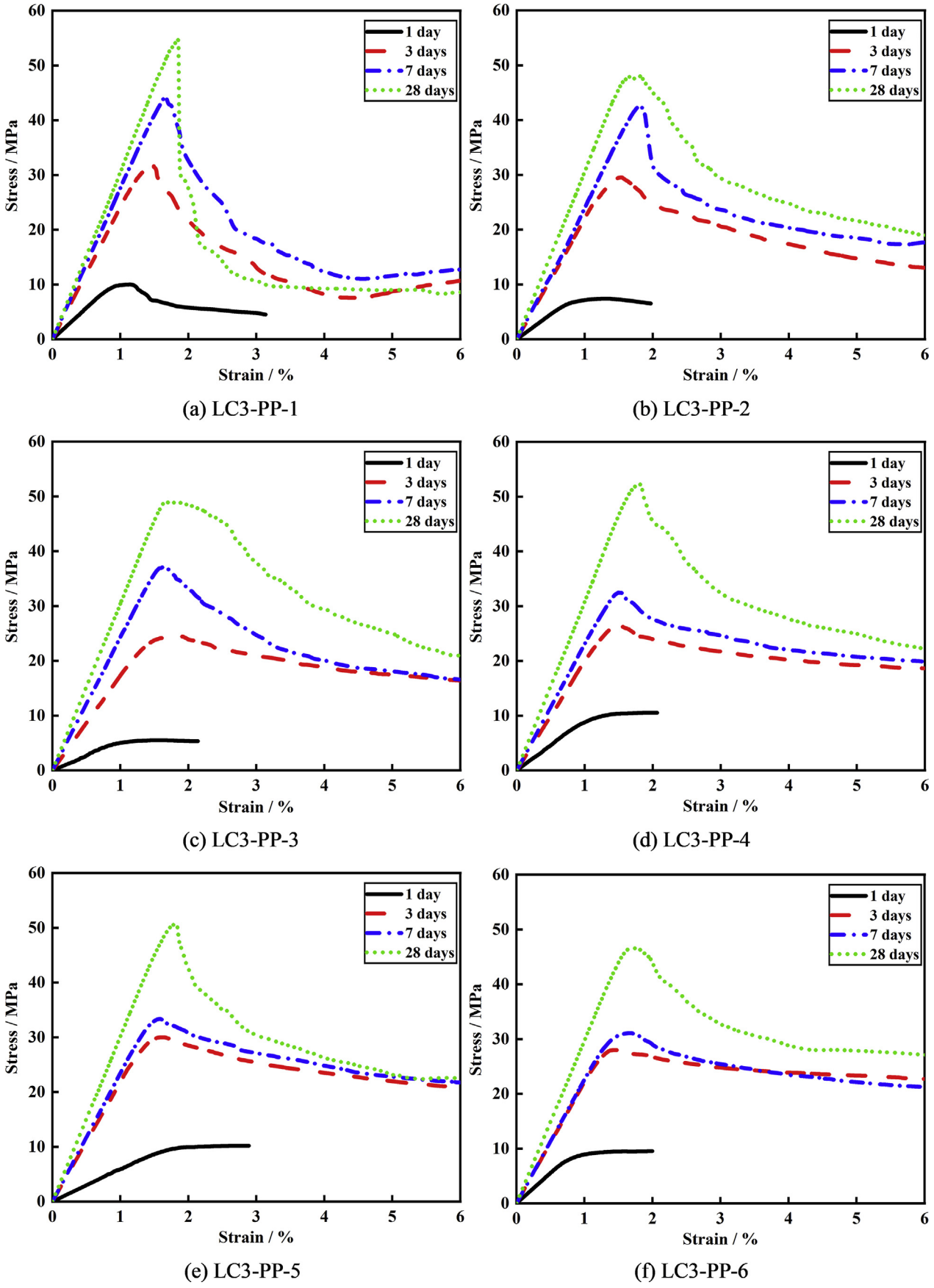

Fig. 6 – σ-ε curves of LC3-PP-ECC groups at different PP fiber contents.

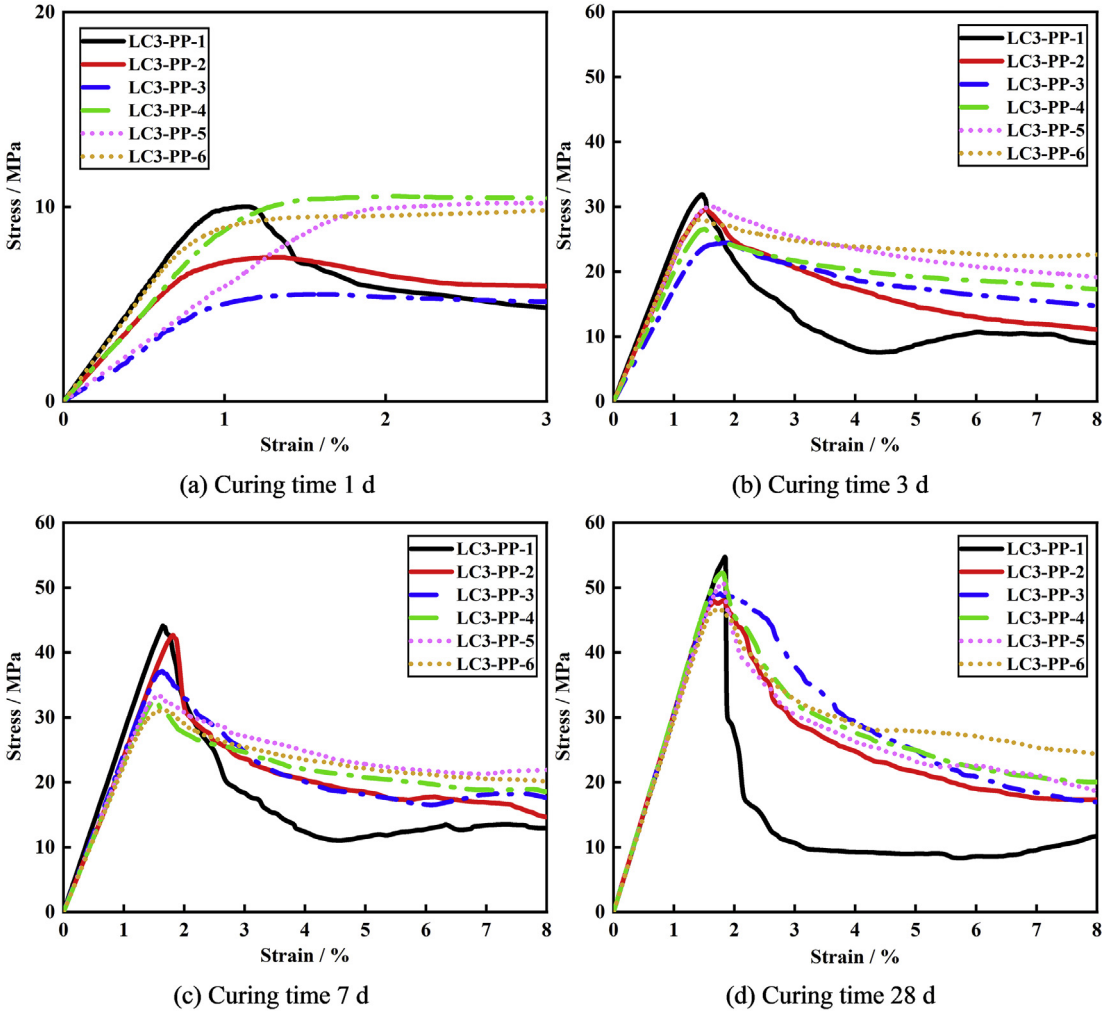

Fig. 7 – Ranges of σ-ε curves of LC3-PP-ECCs at different curing ages and PP fiber contents.

PP fibers, the group with added PP fibers will also have cracks, but there will be no surface peeling.

(3). **BC** stage

Point B is the peak intensity and the data corresponding to the x-axis and y-axis are the peak strain ε_m and the peak stress σ_m values of the specimens. When peak point B is reached, the slope of point B begins to decline and vertical cracks gradually appear on the surface of the specimens at the position of the main oblique cracks. The number of vertical cracks increases with increasing fiber content. These vertical cracks continue to expand, extend and connect and finally form the main oblique cracks. Then, the σ-ε curve reaches point C, which is the inflection point of the curve, that is, the position where the second derivative is 0. The data corresponding to the x-axis and y-axis are the residual strain ε_u and residual stress σ_u of the specimens. In addition, under the 1 d curing age, the specimens containing PP fibers will not produce many cracks when pressed during the compressive process, but the specimens will also be compressed more densely. Therefore, it can be seen in Fig. 8 that, in the stage after point C, some specimens even starting from point B that the σ-ε curve of the LC3-PP specimens will rise abnormally. At the longer curing periods, the LC3-PP-1 specimens without fibers will be seriously damaged when the specimens enter the BC stage (Fig. 8 (b)). The damaged surface of the specimens expands inwardly and then, after peeling off the surface matrix, the shape of the specimens after damage appears as an "apple core" shape and size. In the compressive process, the specimens containing PP fibers will not be completely separated due to the fixation of the PP fibers, but cracks will still occur under compressive loads. There will be obvious separation from the inside of the specimens at a distance of approximately 2 mm from the outside. The size of the area enclosed by the OABC stage and the x-axis is taken as the size of the failure energy A_u, which represents the amount of energy required for the complete failure of the specimens.

(4). **CD** stage

After reaching point C, the lower the fiber content is, the faster the curve of the specimens will drop. For the specimens with a large amount of PP fibers, since the PP fibers are connected to the matrix on both sides of the fractured LC3-ECCs when the cracks develop, the mechanical effect brought by the incorporation of the PP fibers restricts the damage of the matrix. This causes the original brittle failure to be converted to ductile failure. Then, the downward slope of the curve gradually decreases until point D, the curve continues to develop into a horizontal line and the specimens gradually lose their compressive bearing capacity.

3.2.3. *Elastic modulus* E

Fig. 9 shows the elastic modulus values of the six groups of specimens at curing ages of 1 d, 3 d, 7 d and 28 d. It can be clearly observed that, as the curing age increases, the elastic modulus values of each group of specimens continuously increases. At 1 d curing age, the elastic modulus fluctuates with increasing fiber content. The largest were LC3-PP-1 and LC3-PP-6, both of which reached 10.9 GPa. The elastic modulus of LC3-PP-3 is the smallest. At 3 d curing age, the elastic modulus of LC3-PP-3 is the smallest and the values on both sides gradually increase. At 7 d and 28 d curing ages, the general development trend of the elastic modulus is to decrease with increasing PP fibers. The elastic modulus values of LC3-PP-ECCs with PP fiber contents of 0%, 0.5%, 1%, 1.5%, 2% and 2.5%, after 28 d of curing reached 31.3, 29.5, 31.3, 30.3, 30.4 and 27.9 GPa, respectively. LC3-PP-2 and LC3-PP-6 showed lower values. This shows that they produce less stress under the same displacement, and the brittleness is correspondingly smaller.

This study explored the performance of pure LC3 mixtures. The elastic modulus values of LC3-PP-1 at 1 d, 3 d, 7 d and 28 d were 10.9 GPa, 21.7 GPa, 25.1 GPa and 31.3 GPa, respectively. For the LC3 mortar [74], the elastic modulus values corresponding to 1 d, 3 d, 7 d and 28 d are approximately 21 GPa,

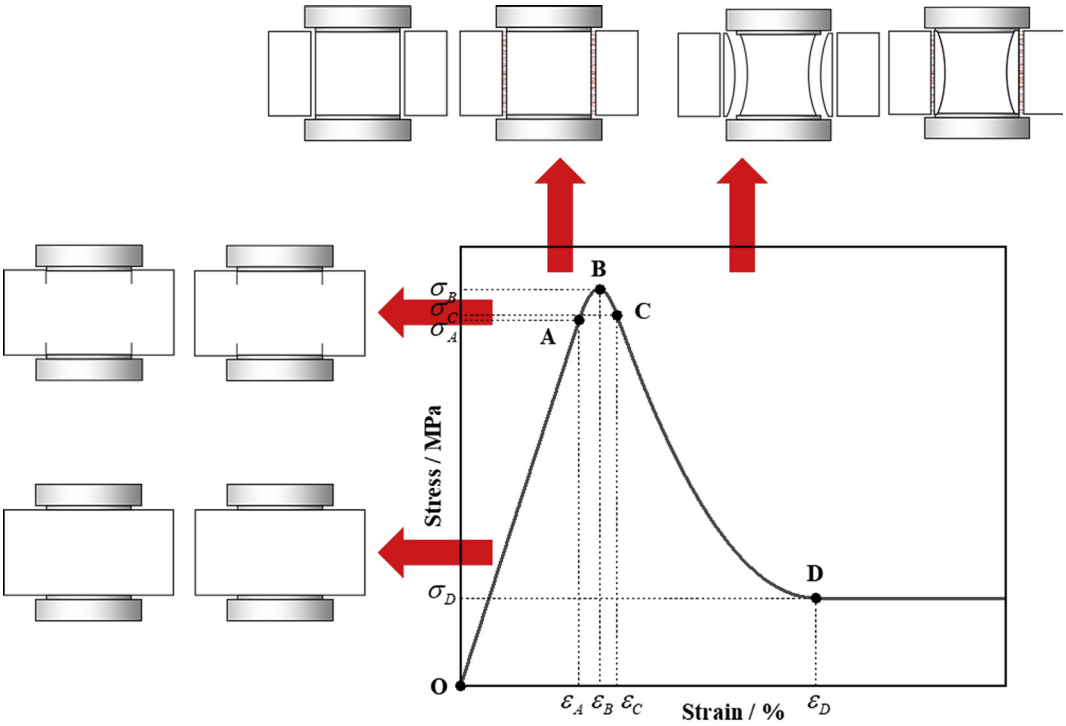

(a) σ-ε curve of LC3-PP-ECCs

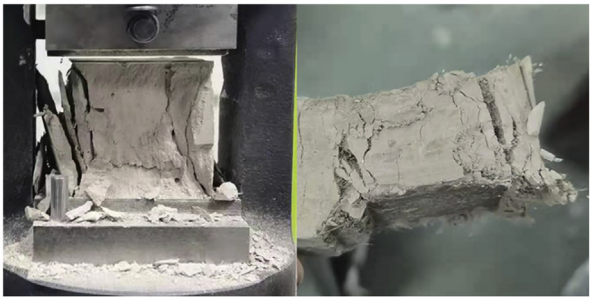

(b) Comparison of the failure patterns of LC3-ECC specimens with and without PP fibers

Fig. 8 – The compressive characteristic of LC3-PP-ECCs.

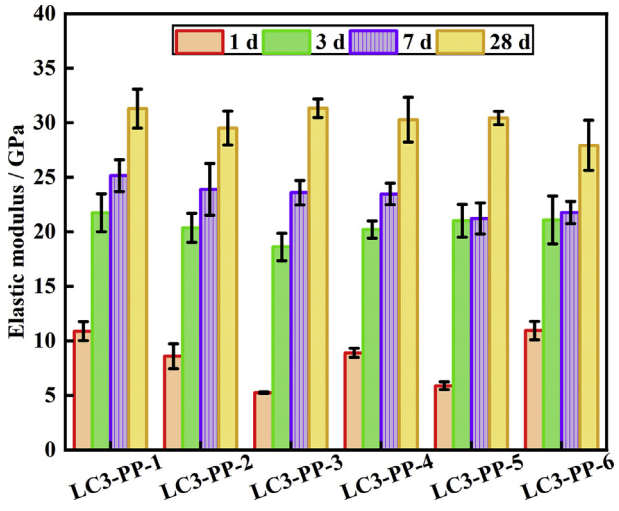

Fig. 9 – Elastic modulus E of LC3-PP-ECCs under curing ages from 1 d to 28 d.

31 GPa, 34 GPa and 34 GPa, respectively. This shows that the elastic modulus of LC3-ECCs basically does not increase after the curing time reaches 7 d, while the elastic modulus of LC3 pastes is still increasing. In addition, the elastic modulus values of LC3-ECCs differed greatly between 1 d and 3 d of curing age. At 28 d, the difference between the LC3-ECCs and LC3 pastes was narrowed to only approximately 3 GPa. PP fibers can appropriately reduce the elastic modulus of the mixtures, thereby impeding the destruction of the mixtures.

3.2.4. *Peak strain and residual strain*

Fig. 10 shows the peak strain ε_m and yield strain ε_u of the LC3-ECCs. Comparing the entire compressive process of 1 d, 3 d, 7 d and 28 d, it can be found that the general change trend of ε_m is rising, while the general change trend of ε_u is relatively flat. For the same curing age, the law between ε_m and PP fiber content has some changes. At 1 d, ε_m increases with increasing fiber content. At 3 d, ε_m is relatively flat with the fiber content, at 7 d and 28 d ε_m decreases with increasing fiber content. The ε_u and ε_m values are roughly the same. At the 28 d curing age, the ε_m values were 1.88%, 1.73%, 1.74%, 1.80%, 1.73% and 1.69% and the ε_u values were 1.92%, 1.80%, 1.81%, 1.89%, 1.87% and 1.80%, for PP fiber contents of 0%, 0.5%, 1%, 1.5%, 2% and 2.5%, respectively. In addition to LC3-PP-1, ε_m and ε_u values of LC3-PP-4 were higher. Among these, the difference between ε_m and ε_u can be regarded as the size of the strain change between the occurrence of cracks and the complete failure of the LC3-ECCs, which represents the length of time that the LC3-ECCs resist damage. The differences between ε_m and ε_u decrease continuously with increasing curing age. At a 28 d curing age, the differences between ε_m and ε_u are 0.04%, 0.07%, 0.07%, 0.09%, 0.14% and 0.11%, for PP fiber contents of 0%, 0.5%, 1%, 1.5%, 2% and 2.5%, respectively. The higher the fiber content shows better values and the best is LC3-PP-5. However, the value of LC3-PP-1 is small, which is the most unfavorable in resisting damage.

Table 3 – Dimensionless eigenvalue.

Curing age	Group	ε_m	σ_m	E	ε_u	σ_u	σ_D
1 d	LC3-PP-1	1.00	1.00	1.31	1.15	0.93	0.49
	LC3-PP-2	1.00	1.00	1.55	1.37	0.95	0.78
	LC3-PP-3	1.00	1.00	1.40	1.22	1.03	0.97
	LC3-PP-4	1.00	1.00	1.26	1.32	0.99	0.99
	LC3-PP-5	1.00	1.00	0.90	1.07	1.00	0.99
	LC3-PP-6	1.00	1.00	1.63	1.19	1.02	1.00
3 d	LC3-PP-1	1.00	1.00	1.16	1.05	0.92	0.32
	LC3-PP-2	1.00	1.00	1.27	1.18	0.92	0.44
	LC3-PP-3	1.00	1.00	1.13	1.33	0.95	0.60
	LC3-PP-4	1.00	1.00	1.18	1.16	0.95	0.62
	LC3-PP-5	1.00	1.00	1.24	1.17	0.98	0.71
	LC3-PP-6	1.00	1.00	1.19	1.14	0.98	0.81
7 d	LC3-PP-1	1.00	1.00	1.08	1.03	0.96	0.26
	LC3-PP-2	1.00	1.00	1.06	1.12	0.93	0.42
	LC3-PP-3	1.00	1.00	1.19	1.08	0.98	0.45
	LC3-PP-4	1.00	1.00	1.11	1.02	0.96	0.56
	LC3-PP-5	1.00	1.00	1.11	1.14	0.97	0.65
	LC3-PP-6	1.00	1.00	1.18	1.09	0.98	0.63
28 d	LC3-PP-1	1.00	1.00	1.01	1.02	0.91	0.16
	LC3-PP-2	1.00	1.00	1.10	1.04	0.94	0.35
	LC3-PP-3	1.00	1.00	1.06	1.04	0.95	0.42
	LC3-PP-4	1.00	1.00	1.06	1.05	0.96	0.40
	LC3-PP-5	1.00	1.00	1.09	1.08	0.96	0.44
	LC3-PP-6	1.00	1.00	1.12	1.06	0.96	0.59

3.2.5. *Peak stress and residual stress*

Fig. 11(a) shows the peak stress of each group of LC3-ECCs. The top values in the red, green, blue and yellow boxes represent the peak stress σ_m at 1 d, 3 d, 7 d and 28 d, respectively. During the 1 d curing process, the three groups with highest PP fiber contents increased faster than the other three groups. Therefore, the three groups with the highest PP fiber contents at 1 d curing age have higher σ_m values than the other three groups. At 3 d and 7 d ages, the σ_m values of the three groups with less fiber content grew faster than those of the three groups with the highest fiber contents, which is different from the situation at 1 d. This corresponds to the peak stress under

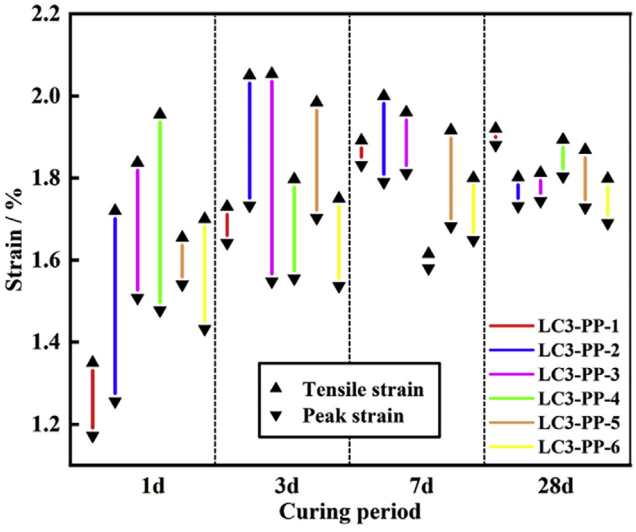

Fig. 10 – The relationship between the peak strain ε_m and the residual strain ε_u of LC3-PP-ECCs at different curing ages.

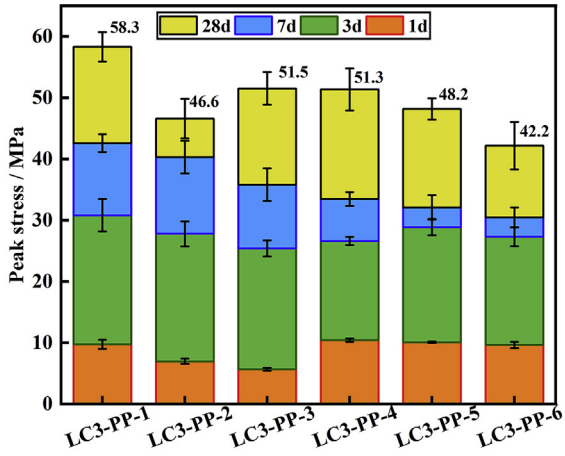

(a) Peak stress σ_m of the LC3-PP-ECCs

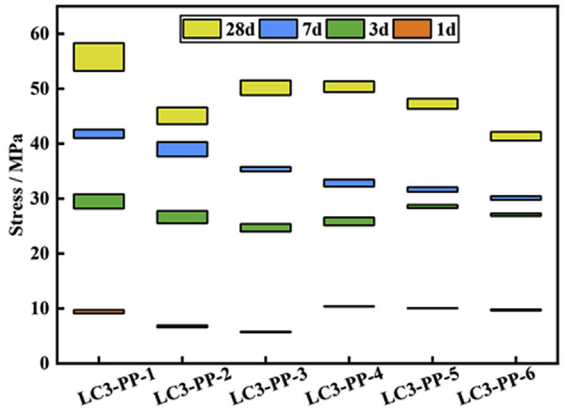

(b) The relationship of the peak stress σ_m and the residual stress σ_u of the LC3-PP-ECCs

Fig. 11 – The peak stress σ_m and the residual stress σ_u of LC3-PP-ECCs at different curing ages.

the curing age, which has a regular decrease with the increase of the fiber content. At 28 days, the increase in the compressive strength of LC3-PP-2 was significantly lower than that of the other groups. The $\boldsymbol{\sigma_m}$ values of the other groups of mixtures decreased with increasing PP fiber content and there were obvious fluctuations in the LC3-PP-2 specimens. This is the result of the combined effect of fibers, hydration products and microstructures. It can be seen from the above phenomenon that when the PP fibers are introduced, the fiber in the early compressive stage can provide part of the compressive resistance, so that the peak strain of the three groups with more PP fiber content in the 1 d curing age is greater. In the later compressive stage, the bearing load is mainly the LC3 matrix, the PP fiber has a smaller effect and the introduced pores or initial flaws caused by the addition of PP fibers into the matrix will reduce the compressive strength of the specimens. Research [75] has shown that the strength of LC3 cementitious material changes little after 28 d of curing age. In this study, the PP fiber does not affect the hydration reaction of LC3. Therefore, it can be considered that the strength of the LC3-PP-ECCs after 28 d of curing will no longer change. The σm values of LC3-PP-1 to LC3-PP-6 are 58.3 MPa, 46.6 MPa, 51.5 MPa, 51.3 MPa, 48.2 MPa and 42.2 MPa, respectively. The σ_m values increase initially and then decrease. Excluding LC3-PP-1, LC3-PP-3 showed the maximum value. The compressive strengths of the LC3 mortar after 3 d, 7 d and 28 d are approximately 15 MPa, 28 MPa and 32 MPa, respectively [65]. Compared with the compressive strength of LC3-PP-1, the compressive strength values of the LC3 pastes are approximately 15 MPa lower than that of the LC3 mixtures over the entire curing age range.

Fig. 11(b) shows the relationship between the peak strain and residual strain. The upper and lower edges in Fig. 11(b) correspond to the values of $\boldsymbol{\sigma_m}$ and $\boldsymbol{\sigma_u}$, respectively. $\boldsymbol{\sigma_u}$ appears in the descending section after $\boldsymbol{\sigma_m}$, so it is slightly smaller than $\boldsymbol{\sigma_m}$ in value. It can be observed that, as the curing age increases, the difference between $\boldsymbol{\sigma_m}$ and $\boldsymbol{\sigma_u}$ increases. With increasing PP fiber content, the difference between $\boldsymbol{\sigma_m}$ and $\boldsymbol{\sigma_u}$

decreases, indicating that the strength of LC3-PP-1 decreases faster.

3.2.6. *Failure energy and toughness*

Fig. 12(a) shows the destruction energy of the LC3-ECCs. The area is obtained by integrating the overall compressive process of the $\boldsymbol{\sigma}$-$\boldsymbol{\varepsilon}$ curves from loading to complete failure, which is used to characterize the failure energy. At a 28 d curing age, the destruction energy of LC3-PP-1 to LC3-PP-6 reached 114.8, 159.3, 182.5, 174.4, 168.4 and 175.2 J, respectively. LC3-PP-3 to LC3-PP-6 show better values and the value of LC3-PP-3 was the best. This measure represents the energy required for the complete destruction of a LC3-PP-ECC specimen. As the curing age increases, its destruction energy also increases. The LC3-PP-1 specimen starts at 3 d and the damage energy increases very slowly. This is because PP fibers are not added to the LC3-PP-1 matrix and it only depends on the matrix itself to absorb energy until it fails. For several groups mixed with PP fibers, the damage energy is significantly greater. This is because the bonding between the PP fibers and the matrix allows more energy to be absorbed until it is broken, which proves that the ECCs with PP fibers have better mechanical performance. However, the damage energy of LC3-PP-2 from 7 d onwards increased more slowly than the other groups. This is the result of less fiber incorporation.

Fig. 12(b) shows the toughness index of the LC3-ECCs, expressed by the area $\boldsymbol{A_d}$ corresponding to the ultimate strain compared to the area $\boldsymbol{A_m}$ corresponding to the upper peak strain. The toughness of LC3-PP-1 basically remains unchanged with increasing curing age. The toughness values of other groups basically increase with increasing curing age. This is because the bond with the PP fibers keep increasing with the curing age, and the bonding degree between the PP fibers and the matrix is better. LC3-PP-1 does not contain PP fibers, so it is less affected by the curing age.

3.3. *LC3-PP-ECCs compressive constitutive relationship*

3.3.1. *Selections of feature points*

To further analyze the structure, a uniaxial compressive stress–strain model is explored in more detail. Before deriving the constitutive relationship, the stress–strain curves are transformed into dimensionless curves by the peak strain $\boldsymbol{\varepsilon_m}$ and the peak stress $\boldsymbol{\sigma_m}$. We observed that the LC3-PP-ECC specimens have the following curve characteristics: Feature (1):$x = 0, y = 0$, the curves always start from the origin point. Feature (2):$x = 0, \frac{dy}{dx} = E_c$, the slope at the origin point corresponds to the dimensionless modulus of elasticity. Feature (3):$x = 1, y = 1$, this point is the peak stress $\boldsymbol{\sigma_m}$ and the peak strain $\boldsymbol{\varepsilon_m}$. Feature (4):$x = 1, \frac{dy}{dx} = 0$, the slope when the curves reach the peak stress is 0. Feature (5):$x = \varepsilon_u, y = \delta_u$, this point corresponds to the residual compressive strength. Feature (6):$x = \varepsilon_u, \frac{d^2y}{dx^2} = 0$, this is the inflection point and the second derivative of the curves is 0. Feature (7):$x = \varepsilon_d, y = \sigma_d$, after this point the specimen loses its load-bearing capacity. Feature (8):$x = \varepsilon_d, \frac{dy}{dx} = C$, after this point the curves enter the linear phase again and the curve slope is constant C.

3.3.2. *Selections of constitutive equation*

Previous studies have proposed a variety of constitutive relationships for the compression of cement-based materials [76–79]. After comparing the characteristics of the constitutive relationships of the LC3-PP-ECCs under uniaxial compression, the following equation was adopted.

Ascending phase equation,

$$y = ax + bx^2 + cx^3 \quad x \le 1 \tag{1a}$$

Downward phase equation,

$$y = Ae^{-B(x-1)^C} + D \quad x > 1 \tag{2a}$$

Among them, a, b, c, A, B, C and D are undetermined parameters.

3.3.3. *Coefficient determination*

In the ascending phase, the three features (2)–(4) are used to solve the three undetermined coefficients a, b and c.

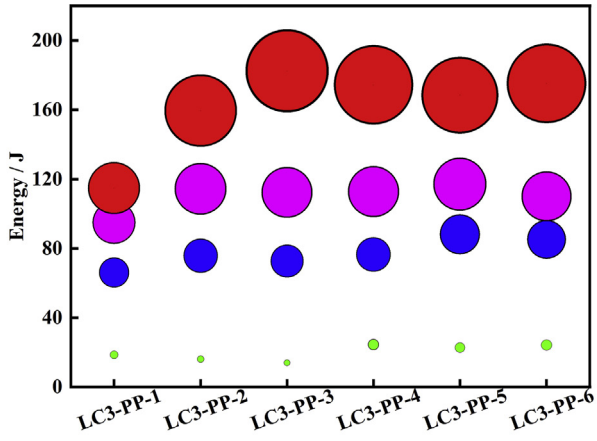

(a) Compressive destructive energy of the LC3-PP-ECCs

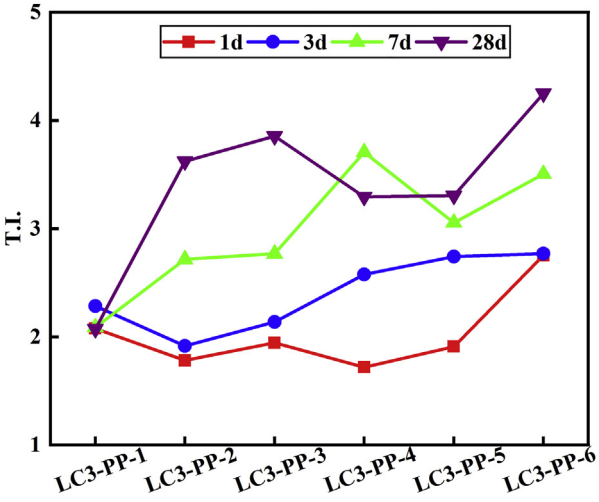

(b) Compressive toughness of LC3-PP-ECCs

Fig. 12 – Compressive toughness and destructive energy of the LC3-PP-ECCs at different curing ages.

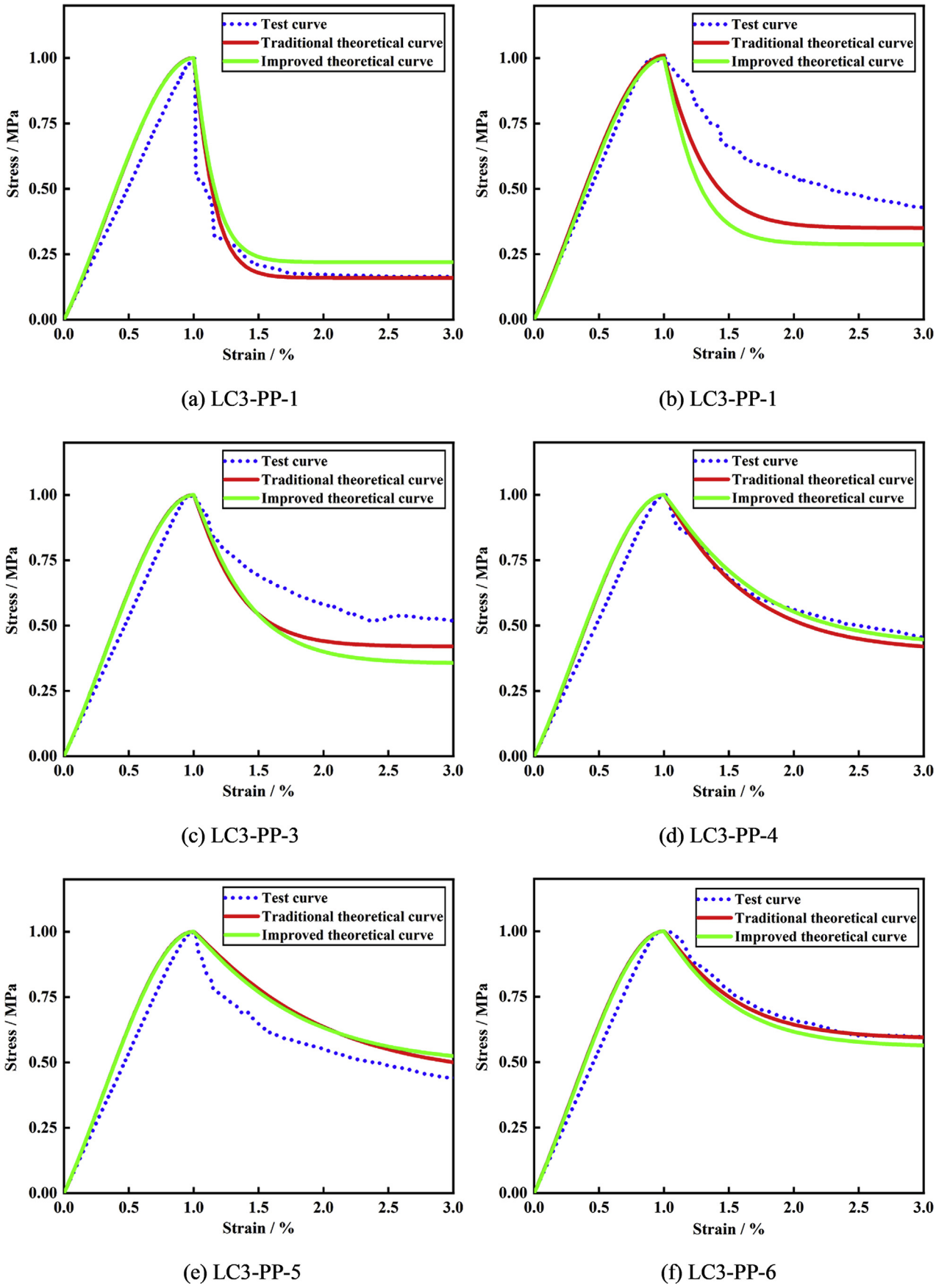

Fig. 13 – Test curves and theoretical curves of the LC3-PP-ECCs after 28 d of curing.

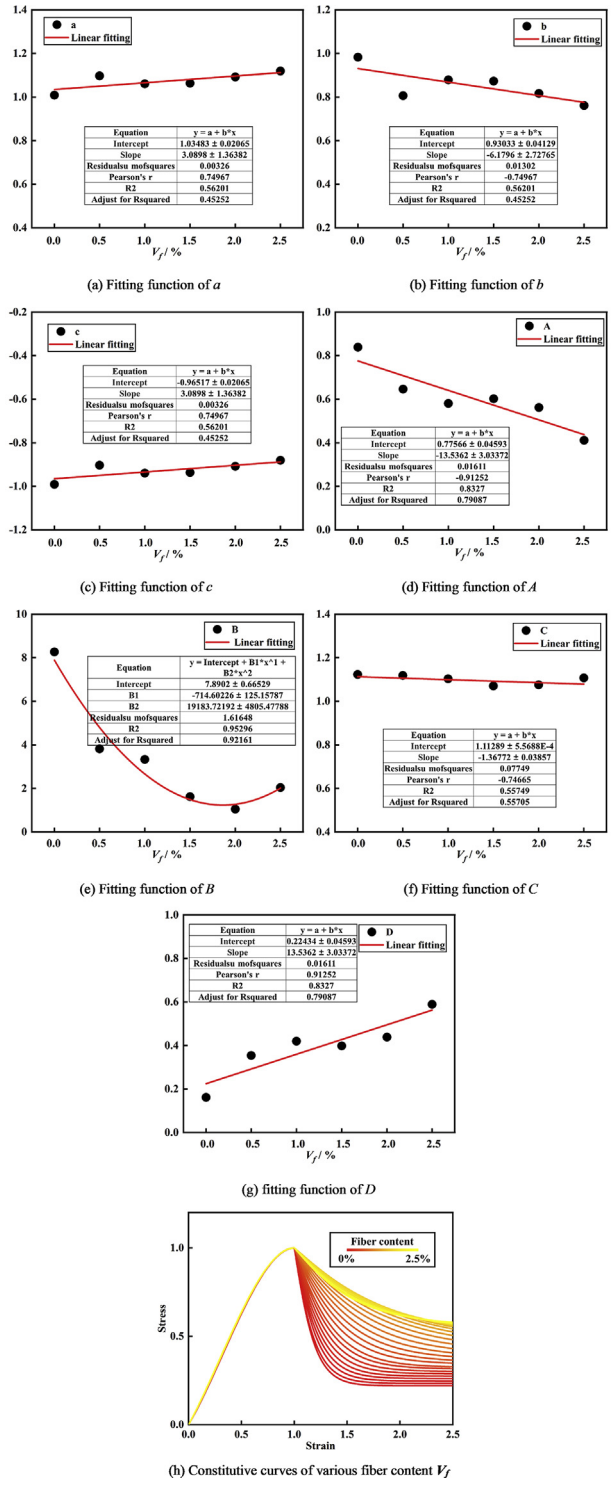

Fig. 14 – Changes in the constitutive equations of the various parameters and fiber content V_f.

(1) $x = 0, \frac{dy}{dx} = E_c$. Substituting into the original formula, $\frac{dy}{dx} = a + 2bx + 3cx^2$,

$$\left.\frac{dy}{dx}\right|_{x=0} = a = \frac{E_c \cdot \varepsilon_m}{\sigma_m} \tag{3}$$

(2) $x = 1, y = 1$. Substituting into the original formula,

$$y|_{x=1} = a + b + c \tag{4}$$

(3) $x = 1, \frac{dy}{dx} = 0$. Substituting into the original formula,

$$\left.\frac{dy}{dx}\right|_{x=1} = a + 2b + 3c = 0 \tag{5}$$

(4) The finishing Equations (1)–(3) are as follows:

$$a = \frac{E_c \cdot \varepsilon_m}{\sigma_m} \tag{6}$$

$$b = 3 - 2a \tag{7}$$

$$c = a - 2 \tag{8}$$

After conversion, the equation of the ascending section is

$$y = ax + (3 - 2a)x^2 + (a - 2)x^3 \quad x \le 1 \tag{9}$$

According to the formula, the curve of the ascending segment is related to E_c, σ_m and ε_m. E_c is directly proportional to ε_m and inversely proportional to σ_m.

In the descending stage, the four feature points of Features (3)–(7) are used to solve for the four undetermined coefficients A, B, C and D.

(5) $x = 1, y = 1$. Substituting into the original equation,

$$y|_{x=1} = A + D = 1 \tag{10}$$

(6) $x = \varepsilon_u, y = \sigma_u$. Substituting into the original equation,

$$y|_{x=\varepsilon_u} = Ae^{-B(\varepsilon_u - 1)^C} + D = \sigma_u \tag{11}$$

(7) $x = \varepsilon_u, \frac{d^2y}{dx^2} = 0$.

(8) $x = \varepsilon_d, y = \sigma_d$. When ε is large enough,

$$D \approx \sigma_d \tag{12}$$

(9) The finishing Equations (5)–(8) are:

Table 4 – Dimensionless coefficient.

Curing age	Group	a	b	c	A	B	C	D
1 d	LC3-PP-1	1.31	0.38	−0.69	0.51	1.24	1.16	0.49
	LC3-PP-2	1.55	−0.10	−0.45	0.22	1.11	1.39	0.78
	LC3-PP-3	1.40	0.21	−0.60	0.03	−1.64	0.60	0.97
	LC3-PP-4	1.26	0.48	−0.74	0.01	3.27	1.78	0.99
	LC3-PP-5	0.90	1.20	−1.10	0.01	3.81	1.20	0.99
	LC3-PP-6	1.63	−0.25	−0.37	0.00	−4.19	0.27	1.00
3 d	LC3-PP-1	1.16	0.68	−0.84	0.68	3.83	1.15	0.32
	LC3-PP-2	1.27	0.46	−0.73	0.56	1.17	1.19	0.44
	LC3-PP-3	1.13	0.73	−0.87	0.40	0.54	1.17	0.60
	LC3-PP-4	1.18	0.64	−0.82	0.38	1.42	1.19	0.62
	LC3-PP-5	1.24	0.52	−0.76	0.29	0.52	1.08	0.71
	LC3-PP-6	1.19	0.63	−0.81	0.19	0.85	1.11	0.81
7 d	LC3-PP-1	1.08	0.84	−0.92	0.74	1.85	1.05	0.26
	LC3-PP-2	1.06	0.88	−0.94	0.58	1.35	1.13	0.42
	LC3-PP-3	1.19	0.61	−0.81	0.55	0.60	1.05	0.45
	LC3-PP-4	1.11	0.78	−0.89	0.44	5.91	1.10	0.56
	LC3-PP-5	1.11	0.78	−0.89	0.35	0.66	1.08	0.65
	LC3-PP-6	1.18	0.65	−0.82	0.37	0.79	1.07	0.63
28 d	LC3-PP-1	1.01	0.98	−0.99	0.84	8.27	1.12	0.16
	LC3-PP-2	1.10	0.81	−0.90	0.65	3.82	1.12	0.35
	LC3-PP-3	1.06	0.88	−0.94	0.58	3.33	1.10	0.42
	LC3-PP-4	1.06	0.87	−0.94	0.60	1.62	1.07	0.40
	LC3-PP-5	1.09	0.82	−0.91	0.56	1.05	1.08	0.44
	LC3-PP-6	1.12	0.76	−0.88	0.41	2.04	1.11	0.59

$$A = 1 - D \tag{13}$$

$$B = \frac{C-1}{C} \bullet \frac{1}{(\varepsilon_u - 1)^c} \tag{14}$$

$$C = \frac{1}{1 + \ln \frac{\sigma_u - D}{A}} \tag{15}$$

$D \approx \sigma_D$ (the type as shown in Equation (12)).

The descending curve is closely related to σ_u, σ_d and ε_u, while D is approximately equal to σ_d, C is inversely proportional to σ_u, B is inversely proportional to ε_u.

The theoretical curve of this equation is the characteristic curve of PP fiber-reinforced LC3 as a cement base at a 28 d curing age. For the curves of 1 d, 3 d and 7 d, the curves will have different changes due to incomplete hydration. If you need to use it, you need to make further corrections.

3.3.4. *Comparison of test curves and theoretical curves*

Before the equations have been completed, the relationship between the coefficients has been calculated. Therefore, we only need to address the values of the E_c, σ_m, ε_m, σ_u, σ_D and ε_u parameters. These parameters are dimensionless, $\sigma_m = 1, \varepsilon_m = 1$. The processed parameters are presented in Table 3. Then, through the equation described in Section 3.3.3, the values of each coefficient are calculated and shown in Table 4.

By continuing to substitute the processed coefficients into the following expressions, the ascending phase equation is the same as Equation (1), and the downward phase equation is the same as Equation (2).

$$y = ax + bx^2 + cx^3 \quad x \le 1 \tag{1b}$$

$$y = Ae^{-B(x-1)^C} + D \quad x > 1 \tag{2b}$$

The deduced theoretical curves and the actually measured test curves are compared and analyzed in Fig. 13(a)–(f), showing the curves of LC3-PP-1 to LC3-PP-6 at 28 d. The red solid line and the blue short dotted line represent the theoretical curves simulated by the equations and parameters and the actual measured curves, respectively.

The rising stage is represented by the linear function, which is relatively close to the test curves shown in Fig. 13. The upward development part will be separated from it, forming a gap. Especially when compared to the groups with a small amount of fibers, the damage occurs more quickly without the bonding effect of the fibers or a small amount of fibers. The slope at the peak changes very fast, so the fitting is not good enough. However, the groups with more PP fiber contents have better ductility, the change at the peak is relatively gentle and the slope at the peak is obviously 0. This is closer to the assumption made when deriving the theoretical curves, so the curves fit more closely.

The equation used for the descending phase $y = Ae^{-B(x-1)^C} + D$. The advantage of this equation is that it can characterize all of the Feature points and there is an inflection point in the descending stage. In addition, the function reaches a constant value that goes on toward infinity, which is also consistent with the law of curve development. Through observation, it can be found that the declining stages of LC3-PP-1, LC3-PP-2 and LC3-PP-3 deviate slightly from the theoretical curves. The main reason is that the characteristics of

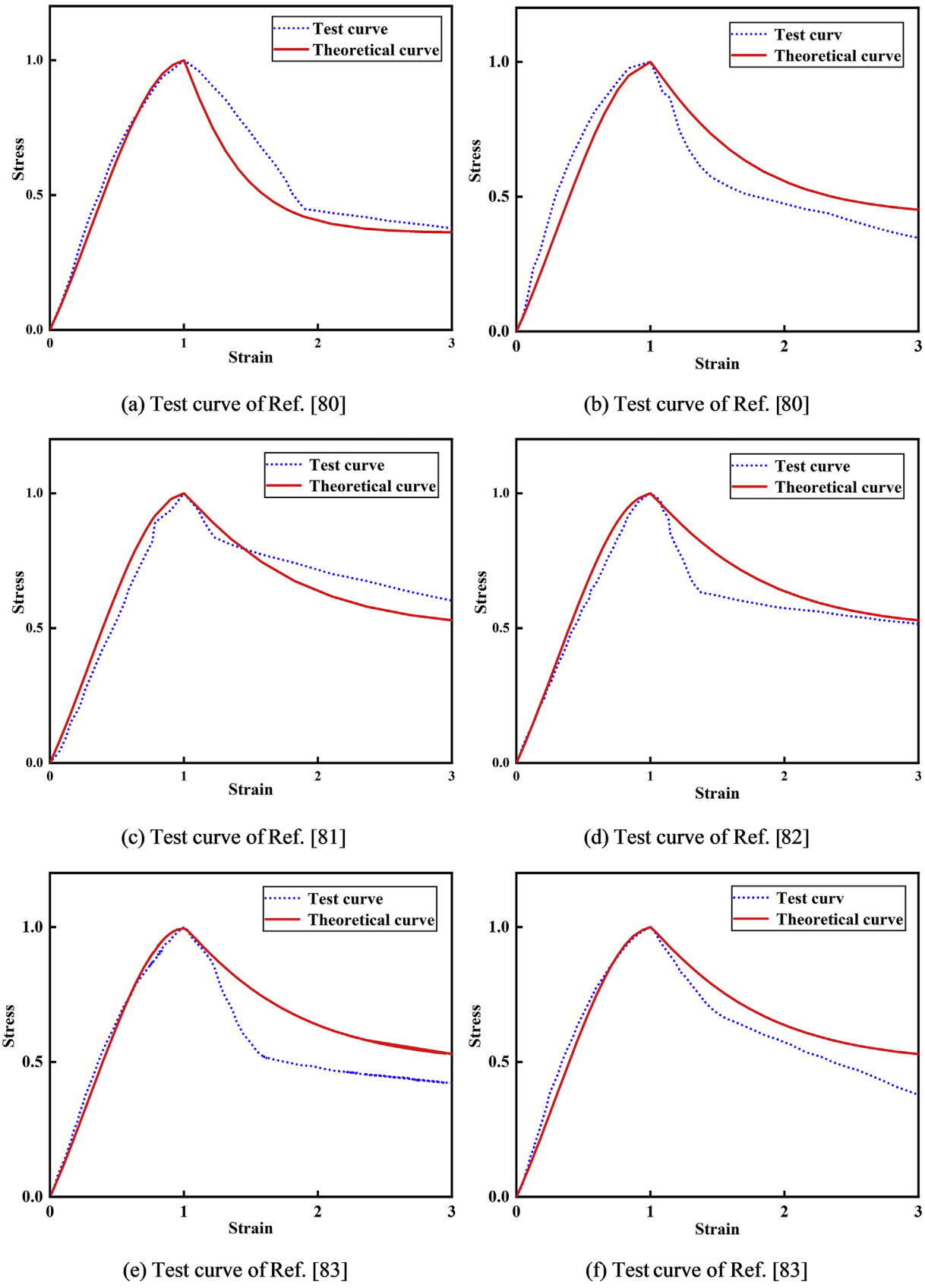

Fig. 15 – Evaluation of the fit of the compressive constitutive model of different fiber contents in other studies.

Table 5 – The parameters of the compressive constitutive equation.

Parameter	*a*	*b*	*c*	*A*	*B*	*C*	*D*
m	1.03	0.93	−0.97	0.78	7.89	1.11	0.22
n	3.09	−6.18	3.09	−13.54	−714.6	−1.37	13.64
l	0	0	0	0	19183.72	0	0

the inflection point are considered in the calculation and the lower the fiber content is, the closer the inflection point is to the peak point and the greater the error in the calculation. Therefore, the theoretical curves of LC3-PP-1, LC3-PP-2 and LC3-PP-3 deviate slightly from the experimental curves. Observing LC3-PP-4, LC3-PP-5 and LC3-PP-6, we found that the curves fit very well. This is because, when the amount of PP fiber is increased, the problems that may occur when the amount of PP fiber is small are avoided and the values between the peak point and the inflection point are larger, so the equation can better reflect the development of the curves.

3.3.5. *Data regression analysis*

The compressive constitutive equation of the LC3-PP-ECCs at a 28 d curing age was obtained. At the same time, *a, b, and c* and *A, B, C,* and *D* were used as parameters to characterize the compressive curves. To further explore the influence of the PP fiber contents on the compressive constitutive model, the PP fiber volume $\mathbf{V_f}$ is used to characterize the parameters *a*, *b*, *c*, *A*, *B*, *C* and *D*, and then $\mathbf{V_f}$ is used to directly express the change in the curves. First, we assume that the expressions of *a*, *b*, *c*, *A*, *B*, *C* and *D* are as follows:

$$i = m_i + n_i \cdot V_f + l_i \cdot V_f^2 \ , \ i = a, b, c, A, B, C, D$$

Through function fitting, the fitting diagrams are shown in Fig. 14. Since *a*, *b*, *c*, *A*, *B*, *C* and *D* meet the requirements of the feature points, *m*, *n* and *r* also meet the requirement of the feature points.

$$\begin{cases} a+b+c=1 \\ a+2b+3c=0 \end{cases} \Rightarrow \begin{cases} m_1+m_2+m_3+n_1 \cdot V_f+n_2 \cdot V_f+n_3 \cdot V_f=1 \\ m_1+2m_2+3m_3+n_1 \cdot V_f+2n_2 \cdot V_f+3n_3 \cdot V_f=0 \end{cases}$$

Based on experience, we adjusted m_3 to −0.96 to meet the requirements. Thus, the values of *a, b, c, A, B, C* and *D* were obtained. The calculated results are shown in Table 5.

Therefore, the relationship equation between σ and V_f is as follows:

$$\begin{cases} \sigma = (1.03+3.09V_f) \cdot x + (0.93-6.18V_f) \cdot x^2 + (-0.97+3.09V_f) \cdot x^3 & x \le 1 \\ \sigma = (0.78-13.54V_f) \cdot e^{-\left(7.89-714.6V_f+19183.72V_f^2\right) \cdot (x-1)^{(1.11-1.37V_f)}} + 0.22 + 13.54V_f & x > 1 \end{cases}$$

The constitutive equation for the range of PP fiber contents between 0% and 2.5% is shown in Fig. 14 (h) and Fig. 13. By observing the green line in Fig. 13, it can be found that the improved theoretical model is more consistent with the experimental curve of this study. This also shows that the improved theoretical curve has some validity and scientific value.

3.3.6. *Comparative verification of theoretical models*

The theoretical equation can effectively express the LC3-PP-ECC compressive constitutive model in this study. We next determine whether it is suitable for different types of PP-ECCs, with reference to other studies [80–83], the $\boldsymbol{\sigma}$-$\boldsymbol{\varepsilon}$ curves of some test pieces are selected. Comparing the constitutive equation of $\mathbf{V_f}$ that has been calculated, the verified results are shown in Fig. 15. It can be observed that, in the rising phase, the experimental curve is very similar to the theoretical curve. However, in the descending stage, the theoretical curve is relatively flat, while the experimental curve will drop sharply. This may be caused by the size and shape of the different ECC specimens. It can be observed that the degree of fitting between the experimental curves and the theoretical curves is relatively good, indicating that the applicability of the suggested constitutive equation is better.

3.4. *XRD analysis*

PP fiber is considered not to chemically react with LC3. Therefore, only LC3-PP-1 was evaluated in the XRD tests. In Fig. 16, the black line, red line, blue line and green line are the XRD test results at curing ages of 1 d, 3 d, 7 d and 28 d, respectively. The peaks in the XRD patterns indicate the crystals present in LC3 at the corresponding curing ages, mainly include calcite (C), calcium hydroxide (CH), ettringite (E), silica (S), hemicarbonate (Hc) and monocarbon aluminate (Mc).

Calcite corresponds to $\boldsymbol{2\theta} = 29°$, and its content increases from 1 d to 3 d and then slowly decreases from 3 d to 28 d. The other types of crystals have lower quantities and no obvious changes. There is basically no change in E because the excessive C in the LC3 system prevents the conversion of E to

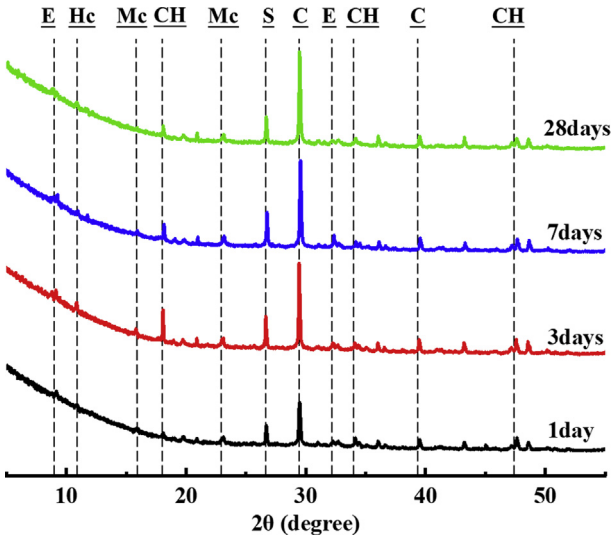

Fig. 16 – XRD patterns of the LC3-PP-ECCs at different curing ages (E: ettringite, C: calcite, S: SiO_2, CH: $Ca(OH)_2$, Mc: monocarboaluminate, Hc: hemicarboaluminate).

Ms [50]. At the same time, the reaction of limestone with additional alumina also prevents E from dissolving to form amorphous Ms [84,85]. The Hc and Mc in the picture can be formed by the reaction of limestone with the activated alumina in C_3A and calcined clay [85]. In addition, the CO_3^{2-} present in the limestone can be substituted for SO_4^{2-} in E and Ms [86]. The resulting carbonate aluminate can improve the mechanical properties of LC3 materials [84]. Previous studies [87] explored the phenomenon of a 3 d curing age, indicating that Mc and Hc phases are formed during the early curing stage. By observing Mc and Hc in Fig. 16, it is found that they have been generated in large quantities at 1 d. This is consistent with the conclusions of the literature [55]. In addition, $2\theta = 18^{\circ}$ corresponds to CH, which obviously decreases from 3 d to 28 d. Because CH will undergo secondary hydration [48], the activated alumina and silica in the calcined clay can react with the CH in the cement, consuming CH and S. It can be seen from the figure that the content of S from 3 d to 28 d decreased slightly and the C-A-S-H gel produced at the same time can increase the mechanical strength of the slurry [88].

3.5. *SEM-EDS analysis*

The SEM images of the damaged surface of the ECCs at approximately 200× magnification are shown in Fig. 17. Fig. 17 (a)-(d) shows the SEM images of the LC3-PP-4, LC3-PP-5, LC3-PP-2 and LC3-PP-5 specimens at curing ages of 1 d, 3 d, 7 d and 28 d, respectively. PP fibers, fiber slip marks, bubbles and pores can be observed in Fig. 17.

PP fibers are randomly distributed in the LC3-PP-ECC matrix and the fiber main ability to withstand external loads is reflected in the drawing slip between the PP fibers and the

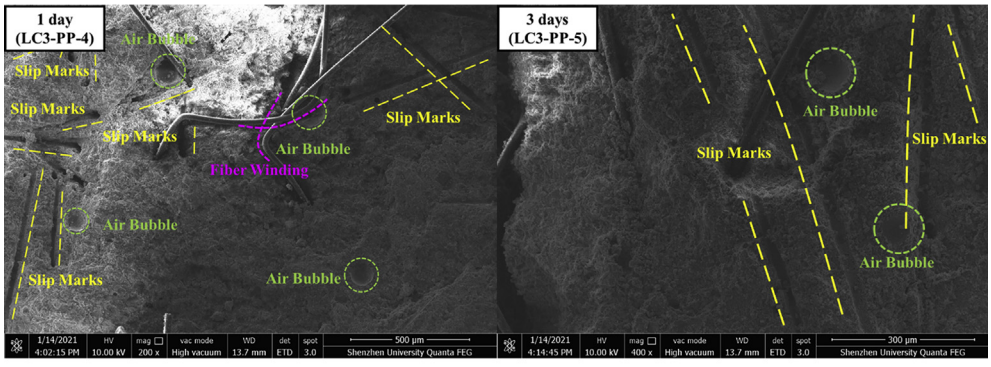

(a) LC3-PP-4 under a 1 d curing age (b) LC3-PP-5 under a 3 d curing age

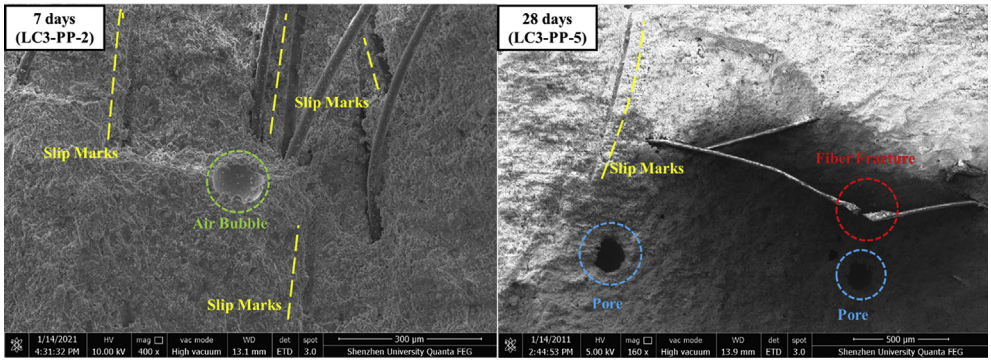

(c) LC3-PP-2 under a 7 d curing age (d) LC3-PP-5 under a 28 d curing age

Fig. 17 – Microstructures of LC3-PP-ECCs at different curing ages.

matrix and the longitudinal tension of the fibers. When the degree of hydration in the ECCs is low, the bond strength between the PP fibers and the matrix is low. If a load is applied at this time, the PP fibers will be pulled out of the matrix. The yellow lines in Fig. 17 mark the traces of PP fibers left on the substrates. However, if the PP fiber is pulled out of the matrix, not only will it leave the pull channels but also flaws or holes will be left, which is obviously detrimental to the compressive performance of the ECCs. When the ECCs have a high degree of hydration, the bonding strength between the PP fibers and the matrix is large enough, which can cause the PP fibers to rupture or fail to provide tensile strength. For example, the red circle in Fig. 17 (d) is the phenomenon in which the PP fiber is broken. The broken end of the PP fibers is obviously not flat. This feature can be used to distinguish whether the PP fiber is pulled out or fractures. By comparison, it can be found that there are obviously more slippage traces than broken PP fibers, which indicates that the failure mode of the PP fibers is more pulled out, which is also mentioned in the literature [65]. A sufficiently high PP fiber content is prone to this phenomenon. For example, the volume content of PP fibers in the ECCs in Fig. 17 (a) reaches 1.5% and there is PP fiber entanglement at the red line mark. At this time, the bridging effect of the PP fiber is no longer a simple interaction with the matrix but also includes the mutual constraint between the PP fibers. In this case, the PP fiber is more likely to break and fail instead of slipping. Therefore, it affects the compressive properties of the ECCs.

There are also a large number of circular bubbles and pores extending to the inside of the ECCs, which are not beneficial for to the mechanical properties of the specimens. Comparing the SEM images in Fig. 17, it can be found that LC-PP-2 with less fiber content has relatively fewer bubbles. This shows that air will be introduced when the PP fiber is added to the pastes and the volume of the gas pores is positively correlated with the volume of the fiber content. This can also be used as a reason to explain the increase in fiber content and the relative decrease in the compressive resistance of the ECCs.

The pictures of the ECC failure surface are shown in Fig. 18, where Fig. 18 (a), (b) and (c) are the images under curing ages of 1 d, 3 d and 7 d, respectively, when the magnification of the SEM is approximately 1500 times. ECCs can significantly change the interaction and cementation between the fiber and the matrix through the fiber/matrix interface, thereby improving the mechanical properties of composite materials [89]. The PP fibers can be mainly observed in Fig. 18 and there are cementitious materials attached to the PP fibers. It not only fills the gaps between the PP fibers and the LC3 matrix but also facilitates the adhesion between the PP fibers and the LC3 matrix. When the materials are destroyed, they will never be completely separated.

Figs. 19–22 show the SEM-EDS chemical element analysis of the ECC damage surface and the SEM-EDS chemical element analysis of the designated substances. The products produced by the LC3 hydration reaction mainly include calcium silicate hydrate (C–S–H), portlandite (CH), ettringite (AFt), monosulfate (AFm), C–S-A-H, and limestone particles [87]. These substances can be found in Figs. 19–22. In addition, pores and cracks can be observed, which cause the microstructures of LC3 to look looser [88].

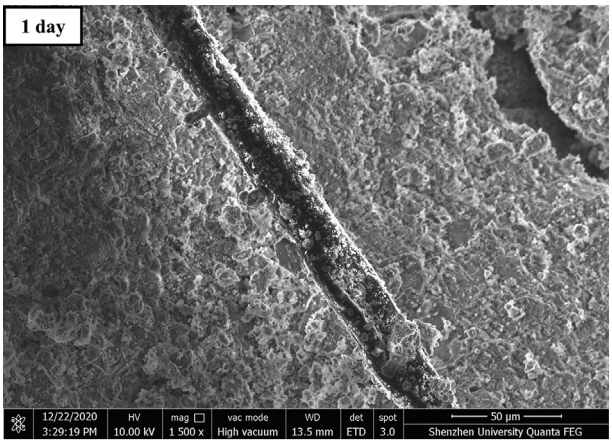

(a) 1 d curing age

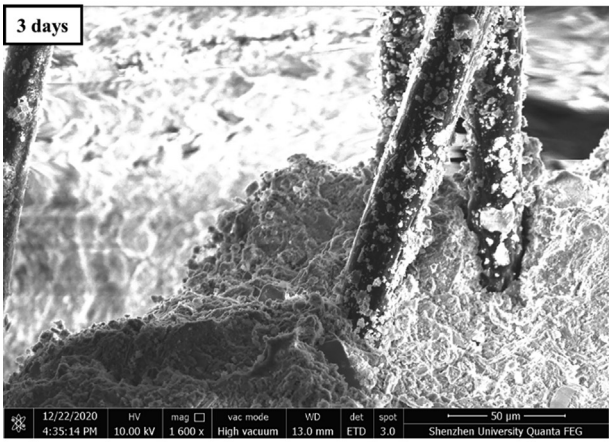

(b) 3 d curing age

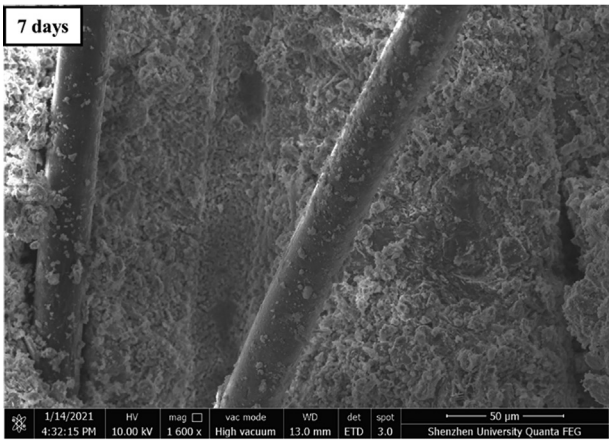

(c) 7 d curing age

Fig. 18 – Microstructures of LC3-PP-ECCs at different curing ages.

In Fig. 19, it can be observed that there are fibrous C–S–H gels, spherical particles and prismatic solids after curing for 1 d, and there are pores and cracks in the matrix. The substances identified in Spot 1 are spherical granular solids. The

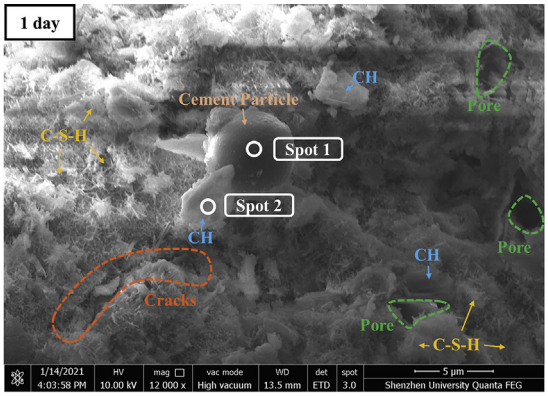

(a) Microstructures of the LC3-PP-ECCs after curing for 1 d

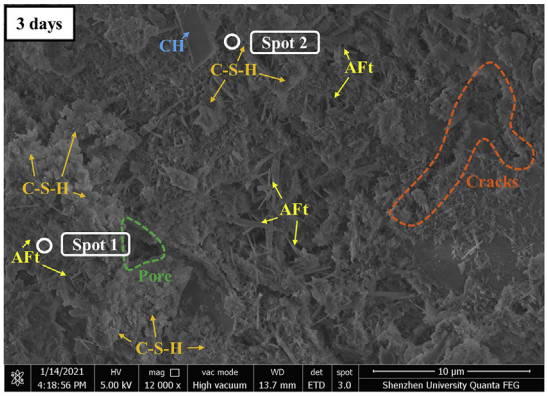

(a) Microstructures of the LC3-PP-ECCs after curing for 3 d

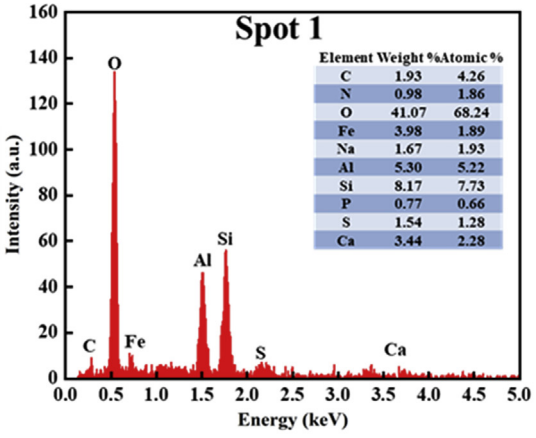

(b) EDS results of Spot 1

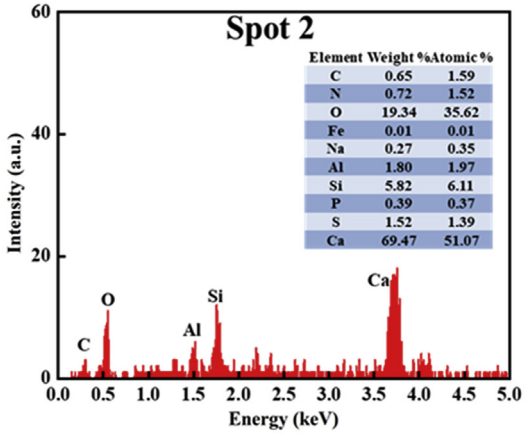

(c) EDS results of Spot 2

Fig. 19 – SEM-EDS images of LC3-PP-ECCs after curing for 1 d.

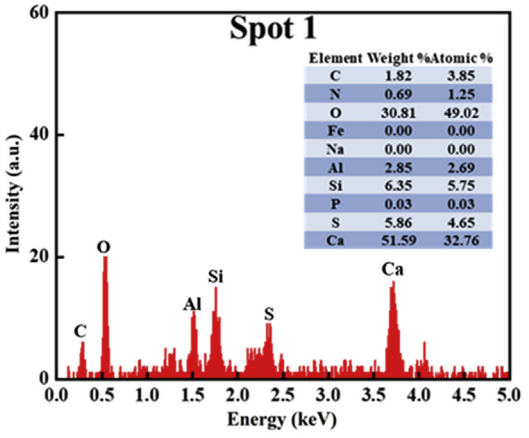

(b) EDS results of Spot 1

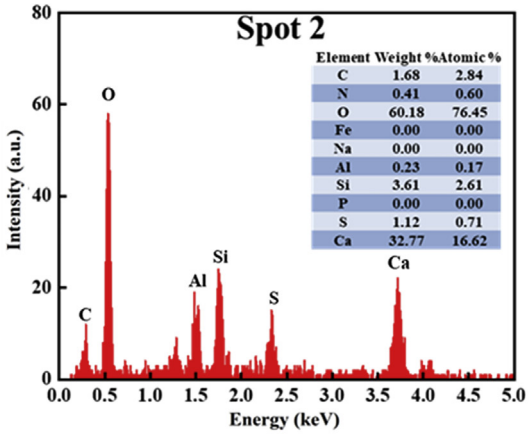

(c) EDS results of Spot 2

Fig. 20 – SEM-EDS images of the LC3-PP-ECCs after curing for 3 d.

SEM-EDS analysis results show that the substances contain more O elements, while other elements are relatively less abundant. It is speculated that the compositions of the substances are mainly oxides, combined with the shape of the substances. Spot 1 was judged to be unhydrated OPC particles. The substance identified at Spot 2 is a prismatic crystal and the SEM-EDS analysis shows that it contains a large amount of O and Ca elements. Therefore, Spot 2 is judged to be CH. In Fig. 20, it can be observed that, after curing for 3 d, except for the products under the 1 d curing age, there are also needle-like prismatic crystals of Aft while needle-like AFt and C–S–H form an interlocking structure [87]. The substance identified at Spot 1 is a needle-shaped crystal. The SEM-EDS

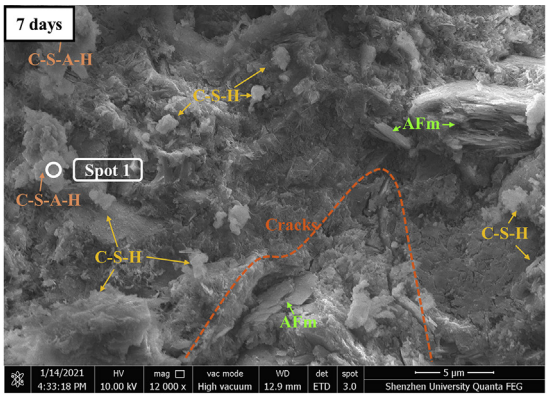

(a) Microstructures of the LC3-PP-ECCs after curing for 7 d

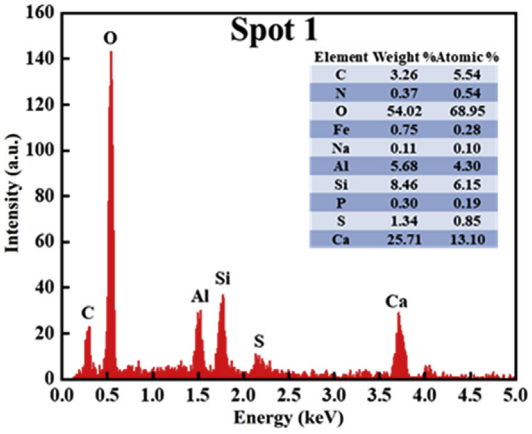

(b) EDS results of Spot 1

Fig. 21 – SEM-EDS images of the LC3-PP-ECCs after curing for 7 d.

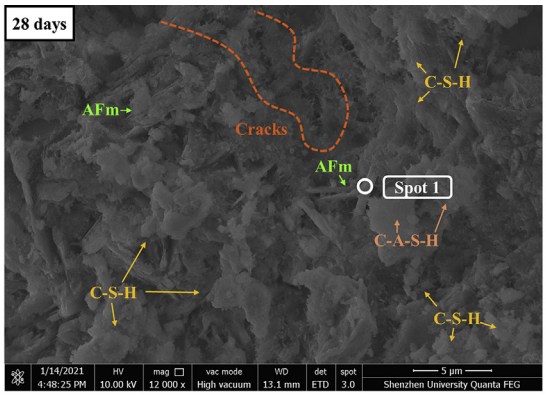

(a) Microstructure of the LC3-PP-ECCs after curing for 28 d

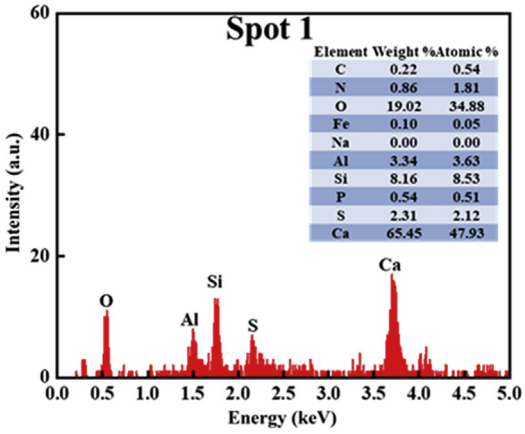

(b) EDS results of Spot 1

Fig. 22 – SEM-EDS images of the LC3-PP-ECC after curing for 28 d.

analysis results show that the substance mainly contains O, Al, Si, S and Ca. It is judged to be AFt gels. By SEM-EDS analysis, the material of Spot 2, was found to mainly contain three elements, O, Si and Ca, and it was determined that the substance was C–S–H gels.

Fig. 21 shows a microscopic picture of the LC3 matrix after curing for 7 days. On the basis of change from the results of the 3 d curing age, new substances such as C-A-S-H gels and flaky AFm crystals have appeared and the amounts of CH and AFt were reduced. With respect to the C-A-S-H gels and CH, after 3 d, the LC3 reacts with the CH to generate more C-A-S-H gels [88,90] and consumes a large amount of CH. This explanation further proves the conclusion that CH in the XRD analysis decreases with increasing curing age. Analysis of Spot 1 by SEM-EDS revealed that the substance mainly contains four elements: O, Al, Si and Ca, which can be judged to be C-A-S-H gels. The active silica and alumina in kaolinite will react with portlandite to form hydrated calcium silicate aluminate C-A-S-H gels and calcium aluminate hydrate C-A-H gels [91], which can fill pores and cracks. Therefore, they contribute to the development of concrete properties [90,92] and enhances the mechanical properties of LC3.

Fig. 22 shows the microstructures of the matrix when cured for 28 d. The types of products are roughly the same as those found at 7 d, but the ECCs are more fully hydrated. The SEM-EDS analysis of Spot 1 shows that the main constituent elements include O, Al, Si, S and Ca. This indicated that the crystal is AFm. Studies have shown that AFm and AFt are due to the high ratio of sulfate to silicate at the beginning of hydration. Therefore, AFt is a hydrate that crystallizes first. When the sulfate is depleted, AFt gels become unstable and gradually convert to AFm gels. Comparing Figs. 19–22, it is easy to find that, as the hydration process progresses, there are crystalline aluminate aggregates and hydrates in the pores [88]. This results in changes in the pore structures of the matrix. In turn, it has an impact on the mechanical properties of LC3-ECCs.

3.6. *Pore analysis*

In this study, the LC3-PP-1, LC3-PP-3 and LC3-PP-5 groups were selected for the MIP test. To further explore the influencing factors of pores, the two sets of ECCs (Ref-1 and Ref-2) in [65] were used as references. Fig. 23 (a) shows the cumulative invasion curve of pores after curing for a 28 d. The cumulative invasion of LC3-PP-1, LC3-PP-3, LC3-PP-5, Ref-1 and

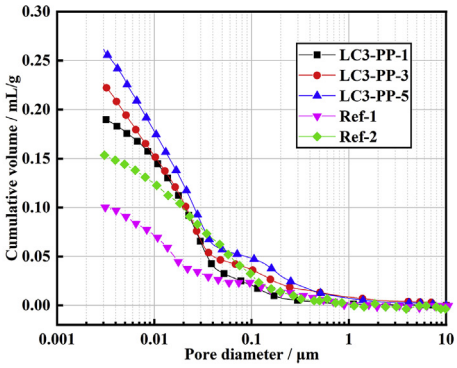

(a) Cumulative pore invasion curve after curing for 28 d

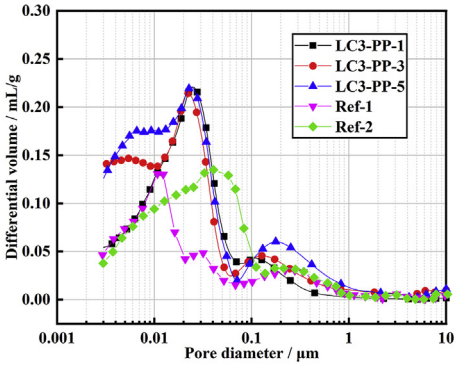

(b) Differential invasion curve of pores after curing for 28 d

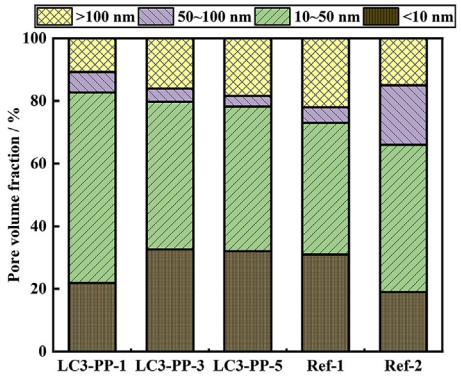

(c) Pore volume fraction after curing for 28 d

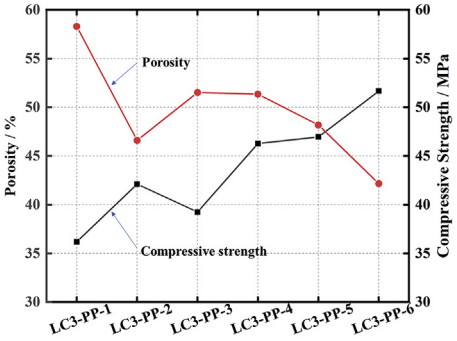

(d) The relationship between the porosity and compressive strength of the LC3-PP-ECC s after curing for 28 d

Fig. 23 – Pore analysis.

Ref-2 reached 0.19, 0.23, 0.26, 0.10 and 0.15 mL/g, respectively. The incorporation of PP fibers increases the porosity. This is due to the lack of cohesiveness of the cement matrix and poor dispersion of the PP fibers, which increases the pore content in the concrete. Toutanji et al. [93,94] also explained this phenomenon in previous studies and found that the addition of PP fibers can also increase the permeability of concrete. It was found [95] that the incorporation of PP fibers makes the pore structure of concrete thicker and, as the content of polypropylene fibers increases, the pore volume and the most likely pore diameter of the concrete (that is, the pore size with the highest frequency) increase. It was also found that, with the increase in PP fibers (LC3-PP-1 to LC3-PP-3 to LC3-PP-5), the cumulative penetration of the pore size increased. This shows that the pore volume and pore size are directly proportional to the fiber content.

The use of auxiliary cementitious materials (SCMs) affects the reaction process in the early stages of hydration and changes the kinetics of microstructure development [96]. Compared with Ref-1 and Ref-2, LC3-PP-ECCs show a larger total porosity (Fig. 23 (a)). The SCM of Ref-1 is FA and the SCMs of Ref-2 are FA and LC3. In [97], the pores of the FA30 and LC3 systems were studied and it was found that, compared with the FA30 system, the LC3 binder has a highly refined pore structure even in the early hydration stage. However, the development of the pore structure in the early hydration stage of FA is slower. However, the rate of LC3 in the later hydration process is slow and the change in pores is relatively small. FA has a better effect than LC3 in the long-term hydration process. Papers [65,98] indicate that mixing fly ash in the LC3 system is also a feasible method.

Fig. 23 (b) shows that the most likely pore diameter (the pore with the highest frequency) of the three groups of LC3-PP-ECCs is maintained at approximately 0.025 μm. This shows that PP fibers do not affect the most likely pore diameter. However, the most likely pore diameter of Ref-1 is approximately 0.01 μm and the most likely pore diameter of Ref-2 is approximately 0.04 μm. This shows that the auxiliary cementing material has an influence on the most likely pore diameter. Ref-2, which is a mixture of LC3 and FA, exhibits a larger critical pore size than when the two gelling materials are used alone. Due to the voids between the fiber surface and the matrix, previous studies [99] stated that adding a 2% volume of PVA fibers can increase the porosity of pores larger than 300 nm by more than 3%. Research [65] believes that, if the fibers can be fully mixed and dispersed in the slurry, the increase in porosity caused by the incorporation of fibers can be minimized. In this study, it can be clearly seen that there are aggregations of pores with a pore size of 200 nm (not reaching 300 nm) (Fig. 23 (b)). This may be the void created between the fiber and the matrix interface. Comparing the porosities of LC3-PP-1, LC3-PP-3 and LC3-PP-5 at 200 nm, it is found that the porosity between the PP fiber and the matrix increases with increasing fiber content. It also shows that full mixing cannot completely offset the existence of pores in the interface zone.

Pores are generally divided into voids (>100 nm), large capillary pores (50–100 nm), medium capillary pores (10–50 nm) and small capillary pores (<10 nm), according to their functions [100]. According to the influence of the pore size on the performance of concrete, the pores can be divided into gel pores (<20 nm), transition pores (20–50 nm), capillary pores (50–200 nm) and macropores (>200 nm) [101]. Fig. 23 (c) shows that, with increasing fiber content (LC3-PP-1 to LC3-PP-3 to LC3-PP-5), the pores and small capillary pores increase. Both the large and medium capillary pores decrease accordingly. However, in general, macropores (harmful pores) are increasing. Compared with the LC3-ECCs, Ref-1 and Ref-2 have a higher proportion of macropores. This shows that LC3 better optimizes the effect on macropores. It is worth noting that macropores and mesopores will affect the mechanical properties and durability of the material. The gel pores and capillary pores mainly affect the shrinkage of the material [102]. In combination with the compressive strength, it can be found that the increase in fiber content leads to an increase in porosity in turn leads to a decrease in the compressive strength of the specimen. Therefore, Fig. 23(d) **shows** that, with increasing fiber content (LC3-PP-1 to LC3-PP-6), the porosity values reached 36%, 42%, 39%, 46%, 47% and 52%, respectively. Generally, there was an increasing trend, and only LC3-PP-2 was abnormal. This proves that the introduction of fibers increases the porosity. With increasing fiber content (LC3-PP-1 to LC3-PP-6), the compressive strength values reached 58 MPa, 47 MPa, 52 MPa, 51 MPa, 48 MPa and 42 MPa, respectively. In general, there was a weakness trend, and only LC3-PP-2 was abnormal. This proves that the introduction of fibers will increase the porosity, thereby reducing the compressive strength of the material. For LC3-PP-2, both the compressive strength and porosity are abnormal, indicating that the effect of the fiber content is poor. At a curing age of 28 d, the porosity of increases approximately 6.5% for every 1% increase in the volume of PP fibers and the compressive strength is reduced about 6.5 MPa.

4. Conclusions

In this study, LC3 was combined with PP fibers to improve the performance of LC3-PP-ECCs. Four different curing ages of 1 d, 3 d, 7 d, 28 d and six different PP fiber volume dosages of 0%, 0.5%, 1%, 1.5%, 2% and 2.5% were tested. The conclusions are as follows:

(1) With increasing curing age, the compressive strength and peak strain of LC3-PP-ECCs will also increase and the compressive strength of the combination and bridging effect with less PP fiber content will rise faster. With increasing PP fiber content, the compressive strength values of LC3-PP-4, LC3-PP-5 and LC3-PP-6 are better at an early curing age. Until 28 d of curing, the compressive strength of theLC3-PP-ECCs basically maintained a downward trend with increasing PP fiber volume. The combined effect of PP fibers and hydration products caused the compressive strength of LC3-PP-2 to drop sharply. The maximum compressive strength of LC3-PP-1 at 28 d can reach 58.3 MPa. Moreover, the specimens with more PP fibers exhibit better toughness and ductility, and the failure energy values of LC3-PP-1 and LC3-PP-2d are relatively low. Among the combinations containing PP fibers, LC3-PP-3 showed better strength, strain and failure energy values. Considering

this comprehensively, it can be considered that it is appropriate to blend PP fibers with a volume content of approximately 1.5% in LC3 cementitious material.

(2) A compressive constitutive model of LC3-PP-ECCs was obtained, it has a good degree of fitting. The equation is also applicable to the compressive constitutive model of other types of ECCs.

(3) XRD analysis results of the surface hydration process show that it will consume a large amount of calcium hydroxide, silica, monocarbon aluminate and semi-carbon aluminate. The resulting C-A-S-H gels can greatly improve the mechanical properties of the ECCs.

(4) In the microstructure, the PP fiber will cause some bubbles or defects in the ECC matrix and the specimens with larger amounts of PP fiber contain relatively more initial cracks or macropores, resulting in a decrease in their compressive strength values. The interaction and bridging effect between the PP fibers and the ECC matrix can also improve its own mechanical properties. The bond effect between the PP fiber and the ECC matrix increases with increasing curing age. In addition, there may be unhydrated cement powders or limestone particles and CH in the early curing stage of LC3-ECCs.

(5) In the late stage of hydration (after 28 days), the total porosity values of the LC3-PP-ECCs are higher than those of ECCs containing fly ash. However, the harmful pores are lower in size than those of ECCs containing fly ash. Cementitious materials have a greater impact on the critical pore size and total porosity. The PP fiber volume has very little effect on the critical pore size but is directly proportional to the total porosity. The main pore size affected are those that are approximately 200 nm. The curing age and fiber content are related to the pore size and compressive strength. The long curing age improves the compressive strength by reducing the macropores. The PP fiber content increases the porosity of the ECCs. At the same time, the total porosity and compressive strength values are almost inversely proportional with a ratio of 1.0.

This study shows that the addition of LC3 is a very effective solution for improving the hydration products of ECCs. Compared with OPC, the mixed cement with 45% LC3 has sufficient compressive strength and lower environmental impact and makes a great contribution to the climate crisis caused by OPC production. Against these background points, these findings can help reduce the carbon footprint of the construction industry. Further research is recommended to reveal the comprehensive performance (uniaxial tensile, durability, fresh properties) of the LC3-ECCs under different w/c ratios or curing conditions, as well as suggestions for using LC3 in actual RC structures.

Data availability

Some or all data, models or code that support the findings of this study are available from the corresponding author upon reasonable request.

Declaration of Competing Interest

The authors declare that they have no known competing financial interests or personal relationships that could have appeared to influence the work reported in this paper.

Acknowledgements

The work described in this paper was fully supported by grants Shenzhen Sustainable Development Technology (Project 2021N031), Shenzhen International Cooperation Research (Project GJHZ20180928155602083) and Provincial Key Laboratory of Durability for Marine Civil Engineering (Project 2020B1212060074).

REFERENCES

[1] Wang Y, Li VC, Backer S. Analysis of synthetic fiber pull-out from a cement matrix. MRS Online Proc Libr 1987;114(1):159–65.

[2] Gao DY, Gu ZQ, Wu C. Bending behavior and deflection prediction of high-strength SFRC beams under fatigue loading. J Mater Res Technol 2020;9(3):6143–59.

[3] Saba AM, Khan AH, Akhtar MN, Khan NA, Koloor SSR, Petrů M, et al. Strength and flexural behavior of steel fiber and silica fume incorporated self-compacting concrete. J Mater Res Technol 2021;12:1380–90.

[4] Chun B, Shin W, Jang YS, Yoo DY. Developing strain-hardening ultra-rapid-hardening mortar containing high-volume supplementary cementitious materials and polyethylene fibers. J Mater Res Technol 2021;13:1934–45.

[5] Gao D, Lv M, Yang L, Tang J. Flexural properties of high ductility cementitious composites with totally recycled fine aggregate. J Mater Res Technol 2021;14:1319–32.

[6] Zeyad AM, Khan AH, Tayeh BA. Durability and strength characteristics of high-strength concrete incorporated with volcanic pumice powder and polypropylene fibers. J Mater Res Technol 2020;9(1):806–18.

[7] Sandiani M, Tanzadeh J. Laboratory assessing of the liquefaction potential and strength properties of Sand soil treated with mixture of nanoclay and glass fiber under dynamic and static loading. J Mater Res Technol 2020;9(6):12661–84.

[8] Qu F, Li W, Tang Z, Wang K. Property degradation of seawater sea sand cementitious mortar with GGBFS and glass fiber subjected to elevated temperatures. J Mater Res Technol 2021;13:366–84.

[9] Jiang D, Jiang D, Lv S, Cui S, Sun S, Song X, et al. Effect of modified wheat straw fiber on properties of fiber cement-based composites at high temperatures. J Mater Res Technol 2021;14:2039–60.

[10] Jiang D, Lv S, Cui S, Sun S, Song X, He S, An P. Effect of thermal insulation components on physical and mechanical properties of plant fibre composite thermal insulation mortar. J Mater Res Technol 2020;9(6):12996–3013.

[11] Wei H, Liu T, Zhou A, Zou D, Liu Y. Multiscale insights on enhancing tensile properties of ultra-high performance cementitious composite with hybrid steel and polymeric fibers. J Mater Res Technol 2021;14:743–53.

[12] Tinoco MP, de Andrade Silva F. On the mechanical behavior of hybrid fiber reinforced strain hardening cementitious

composites subjected to monotonic and cyclic loading. J Mater Res Technol 2021;11:754–68.
[13] Li VC, Wu C, Wang S, Ogawa A, Saito T. Interface tailoring for strain-hardening polyvinyl alcohol-engineered cementitious composite (PVA-ECC). Mater J 2002;99:463–72.
[14] Yang E-H, Sahmaran M, Yang Y, Li VC. Rheological control in production of engineered cementitious composites. ACI Mater J 2009;106:357.
[15] Li VC. Engineered cementitious composites (ECC): bendable concrete for sustainable and resilient infrastructure. Springer; 2019.
[16] Weimann M, Li VC. Hygral behavior of engineered cementitious composites (ECC). Int J Restor Build Monum 2003;9:513–34.
[17] Li VC. Engineered cementitious composites (ECC)–material, structural, and durability performance. Concre Construct Eng Handbook 2008:1–78.
[18] Li VC. On engineered cementitious composites (ECC). J Adv Concr Technol 2003;1:215–30.
[19] Liu H, Zhang Q, Li VC, Su H, Gu C. Durability study on engineered cementitious composites (ECC) under sulfate and chloride environment. Construct Build Mater 2017;133:171–81.
[20] Lepech MD, Li VC. Long term durability performance of engineered cementitious composites/langzeitbeständigkeit systematisch entwickelter zusammengesetzter zement gebundener werkstoffe. Restor Build Monum 2006;12:119–32.
[21] Li VC. Tailoring ECC for special attributes: a review. Int J Concr Struct Mater 2012;6:135–44.
[22] Lepech MD, Li VC, Robertson RE, Keoleian GA. Design of green engineered cementitious composites for improved sustainability. ACI Mater J 2008;105:567.
[23] Li VC, Lepech MD, Wang S, Weimann M, Keoleian GA. Development of green ECC for sustainable infrastructure systems. 2004.
[24] Baiano C, Schiavo E, Gerbaldi C, Bella F, Meligrana G, Talarico G, Muñoz-García AB. Role of surface defects in CO2 adsorption and activation on CuFeO2 delafossite oxide. Molecul Cataly 2020;496:111181.
[25] Mohammed A, Rafiq S, Sihag P, Kurda R, Mahmood W, Ghafor K, et al. ANN, M5P-tree and nonlinear regression approaches with statistical evaluations to predict the compressive strength of cement-based mortar modified with fly ash. J Mater Res Technol 2020;9(6):12416–27.
[26] Mehta PK. High-performance, high-volume fly ash concrete for sustainable development. In: Proceedings of the international workshop on sustainable development and concrete technology. Ames, IA, USA: Iowa State University; 2004. p. 3–14.
[27] Qadir W, Ghafor K, Mohammed A. Regression analysis and Vipulanandan model to quantify the effect of polymers on the plastic and hardened properties with the tensile bonding strength of the cement mortar. Result Mater 2019:100011.
[28] Choi YC, Park B. Effects of high-temperature exposure on fractal dimension of fly-ash-based geopolymer composites. J Mater Res Technol 2020;9(4):7655–68.
[29] Wu HL, Zhang D, Ellis BR, Li VC. Development of reactive MgO-based Engineered Cementitious Composite (ECC) through accelerated carbonation curing. Construct Build Mater 2018;191:23–31.
[30] Zhu H, Zhang D, Wang T, Wu H, Li VC. Mechanical and self-healing behavior of low carbon engineered cementitious composites reinforced with PP-fibers. Construct Build Mater 2020;259:119805.
[31] Hosan A, Shaikh FUA. Compressive strength development and durability properties of high volume slag and slag-fly ash blended concretes containing nano-CaCO3. J Mater Res Technol 2021;10:1310–22.
[32] Souza AT, Barbosa TF, Riccio LA, dos Santos WJ. Effect of limestone powder substitution on mechanical properties and durability of slender precast components of structural mortar. J Mater Res Technol 2020;9(1):847–56.
[33] Yang KH, Jung YB, Cho MS, Tae SH. Effect of supplementary cementitious materials on reduction of CO2 emissions from concrete. Handb Low Carbon Concret 2017:89–110.
[34] Crossin E. The greenhouse gas implications of using ground granulated blast furnace slag as a cement substitute. J Clean Prod 2015;95:101–8.
[35] Saha AK, Khan MNN, Sarker PK, Shaikh FA, Pramanik A. The ASR mechanism of reactive aggregates in concrete and its mitigation by fly ash: a critical review. Construct Build Mater 2018;171:743–58.
[36] Siddique R. Utilization of silica fume in concrete: review of hardened properties. Resour Conserv Recycl 2011;55:923–32.
[37] Khan MI, Siddique R. Utilization of silica fume in concrete: review of durability properties. Resour Conserv Recycl 2011;57:30–5.
[38] Özbay E, Erdemir M, Durmuş Hİ. Utilization and efficiency of ground granu-lated blast furnace slag on concrete properties – a review. Construct Build Mater 2016;105:423–34.
[39] Yu J, Leung CKY. Strength improvement of strain-hardening cementitious composites with ultrahigh-volume fly ash. J Mater Civ Eng 2017;29:05017003.
[40] Şahmaran MS, Li VC. Durability properties of micro-cracked ECC containing high volumes fly ash. Cement Concr Res 2009;39:1033–43.
[41] Zhu Y, Yang Y, Yao Y. Use of slag to improve mechanical properties of engineered cementitious composites (ECCs) with high volumes of fly ash. Construct Build Mater 2012;36:1076–81.
[42] Choucha S, Benyahia A, Ghrici M, Mansour MS. Effect of natural pozzolan content on the properties of engineered cementitious composites as repair material. Front Struct Civ Eng 2018;12:261–9.
[43] Shoba KB, Asha P. Study on engineered cementitious composites using micro silica & polypropylene fibre. Int J Civ Eng Technol 2018;97:1581–9.
[44] Zhou J, Qian S, Beltran MGS, Ye G, Breugel K, Li VC. Development of engineered cementitious composites with limestone powder and blast furnace slag. Mater Struct 2010;43:803–14.
[45] Lothenbach B, Scrivener K, Hooton R. Supplementary cementitious materials. Cement Concr Res 2011;41:217–29.
[46] Muzenda TR, Hou P, Kawashima S, Sui T, Cheng X. The role of limestone and calcined clay on the rheological properties of LC3. Cement Concr Compos 2020;107:103516.
[47] Nematollahi B, Sanjayan J, Shaikh FUA. Synthesis of heat and ambient cured one-part geopolymer mixes with different grades of sodium silicate. Ceram Int 2015;41:5696–704.
[48] Scrivener K, Favier A. Calcined clays for sustainable concrete, vol. 10. Rilem bookseries; 2015.
[49] de Haro JC, Tatsi E, Fagiolari L, Bonomo M, Barolo C, Turri S, et al. Lignin-based polymer electrolyte membranes for sustainable aqueous dye-sensitized solar cells. ACS Sustainable Chem Eng 2021;9:8550–60.
[50] Lothenbach B, Saout GL, Gallucci E, Scrivener K. Influence of limestone on the hydration of Portland cements. Cement Concr Res 2008;38:339–56.
[51] Palm S, Proske T, Rezvani M, Hainer S, Müller C, Graubner C. Cements with a high limestone content – mechanical properties, durability and ecological characteristics of the concrete. Construct Build Mater 2016;119:308–18.

[52] Michael T, Anik D, Bruce B, Laurent B. Equivalent durability performance of Portland limestone cement. Concr Int 2013;35:39–65.
[53] Weerdt KD, Haha MB, Saout GL, Kjellsen KO, Justnes H, Lothenbach B. Hydration mechanisms of ternary Portland cements containing limestone powder and fly ash. Cement Concr Res 2011;41:279–91.
[54] John VM, Damineli BL, Quattrone M, Pileggi RG. Fillers in cementitious materials — experience, recent advances and future potential. Cement Concr Res 2018;114:65–78.
[55] Antoni M, Rossen J, Martirena F, Scrivener K. Cement substitution by a combination of metakaolin and limestone. Cement Concr Res 2012;42:1579–89.
[56] Sui S, Georget F, Maraghechi H, Sun W, Scrivener K. Towards a generic approach to durability: factors affecting chloride transport in binary and ternary cementitious materials. Cement Concr Res 2019;124:05783.
[57] Dhandapani Y, Sakthivel T, Santhanam M, Gettu R, Pillai RG. Mechanical properties and durability performance of concretes with limestone calcined clay cement (LC3). Cement Concr Res 2018;107:136–51.
[58] Scrivener K, Martirena F, Bishnoi S, Maity S. Calcined clay limestone cements (LC3). Cement Concr Res 2017;114:49–56.
[59] He C, Osbaeck B, Makovicky E. Pozzolanic reactions of six principal clay minerals: activation, reactivity assessments and technological effects. Cement Concr Res 1995;25:1691–702.
[60] Alujas A, Fernández R, Quintana R, Scrivener KL, Martirena F. Pozzolanic reactivity of low grade kaolinitic clays: influence of calcination temperature and impact of calcination products on OPC hydration. Appl Clay Sci 2015;108:94–101.
[61] Avet F, Scrivener K. Investigation of the calcined kaolinite content on the hydration of limestone calcined clay cement (LC3). Cement Concr Res 2018;107:124–35.
[62] Berriel SS, Favier A, Domínguez ER, Machado IRS, Heierli U, Scrivener K, et al. Assessing the environmental and economic potential of limestone calcined clay cement in Cuba. J Clean Prod 2016;124:361–9.
[63] Emmanuel AC, Haldar P, Maity S, Bishnoi S. Second pilot production of limestone calcined clay cement in India: the experience. Indian Concr J 2016;90:57–64.
[64] Zhu H, Yu K, Li VC. Sprayable engineered cementitious composites (ECC) using calcined clay limestone cement (LC3) and PP fiber – ScienceDirect. Cement Concr Compos 2021;115:103868.
[65] Zhang D, Jaworska B, Zhu H, Dahlquist K, Li VC. Engineered Cementitious Composites (ECC) with limestone calcined clay cement (LC3). Cement Concr Compos 2020;114:103766.
[66] Yu J, Wu H, Leung CK. Feasibility of using ultrahigh-volume limestone-calcined clay blend to develop sustainable medium-strength Engineered Cementitious Composites (ECC). J Clean Prod 2020;262:121343.
[67] GB 175-2007 General purpose portland cement. Beijing, China: Chinese National Standard; 1999 [In Chinese].
[68] Jin H, Yang S, Xu H, Xu Z, Li F, Tian Y, et al. Uniaxial tensile performance of PP-ECC: effect of curing temperatures and fly ash contents. KSCE J Civil Eng 2020;24(11):3435–46. https://doi.org/10.1007/s12205-020-0402-x.
[69] Ferreiro S, Herfort D, Damtoft J. Effect of raw clay type, fineness, water-to-cement ratio and fly ash addition on workability and strength performance of calcined clay – limestone Portland cements. Cement Concr Res 2017;101:1–12.
[70] GB/T 17671-1999, Cement mortar strength test method (ISO method) [In Chinese].
[71] Cai Ziwei, Liu Feichi, Yu Jiangtao, Yu Kequan, Tian Likang. Development of ultra-high ductility engineered cementitious composites as a novel and resilient fireproof coating. Construct Build Mater 2021;288:123090.
[72] Jin H, Liu J, Jiang Z, Zhou H, Liu J. Influence of the rainfall intensity on the chloride ion distribution in concrete with different levels of initial water saturation. Construct Build Mater 2021;281:122561.
[73] Liu J, Ou G, Qiu Q, Chen X, Hong J, Xing F. Chloride transport and microstructure of concrete with/without fly ash under atmospheric chloride condition. Construct Build Mater 2017;146:493–501.
[74] Du H, Pang SD. High-performance concrete incorporating calcined kaolin clay and limestone as cement substitute. Construct Build Mater 2020;264:120152.
[75] Yu J, Wu HL, Mishra DK, Li G, Leung CK. Compressive strength and environmental impact of sustainable blended cement with high-dosage Limestone and Calcined Clay (LC2). J Clean Prod 2021;278:123616.
[76] Sargin M. Stress-strain relationship for concrete and the analysis of structural concrete sections. 1971.
[77] Minervino E, Minervino E. Stress-strain curves of normal and lightweight concrete in compression. Int J Rock Mech Min Sci Geomech Abstr 1979;16:146.
[78] Rusch H. Researches toward a general flexural theory for structural concrete. J Proceed 1960;57.
[79] Hognestad E, Hanson NW, McHenry D. Concrete stress distribution in ultimate strength design. J Proceed 1955;52.
[80] Wang Z, Zhou J, Zhang X, Jiang G, Feng L. Stress-strain behavior of hybrid-fiber engineered cementitious composite in compression. Adv Cement Res 2018;32:1–61.
[81] Li L, Bai Y, Yu K, Yu J, Lu Z. Reinforced high-strength engineered cementitious composite (ECC) columns under eccentric compression: experiment and theoretical model. Eng Struct 2019;198:109541.
[82] Zhou J, Pan J, Leung CKY. Mechanical behavior of fiber-reinforced engineered cementitious composites in uniaxial compression. J Mater Civ Eng 2015;27:1.
[83] Ding Y, Yu K, Mao W. Compressive performance of all-grade engineered cementitious composites: experiment and theoretical model. Construct Build Mater 2020;244:118357.
[84] Bonavetti VL, Rahhal VF, Irassar EF. Studies on the carboaluminate formation in limestone filler-blended cements. Cement Concr Res 2001;31:853–9.
[85] Matschei T, Lothenbach B, Glasser FP. The AFm phase in Portland cement. Cement Concr Res 2007;37:118–30.
[86] Okoronkwo MU, Glasser FP. Compatibility of hydrogarnet, Ca3Al2(SiO4)x(OH)4(3-x), with sulfate and carbonate-bearing cement phases: 5-85 °C. Cement Concr Res 2016;83:86–96.
[87] Tiwari AK, Chowdhury S. Relative evaluation of performance of limestone calcined clay cement compared with Portland pozzolana cement. J Asian Concret Feder 2016;2:110–6.
[88] Li Q, Li Wx, Hou P, Heng C, Yang W, Xin C. The microstructure and mechanical properties OF cementitious materials comprised OF limestone, calcined clay and clinker. Ceramics 2019;63:356–64.
[89] Karger-Kocsis J, Mahmood H, Pegoretti A. Recent advances in fiber/matrix interphase engineering for polymer composites. Prog Mater Sci 2015;73:1–43.
[90] Avet F, Boehm-Courjault E, Scrivener K. Investigation of C-A-S-H composition, morphology and density in limestone calcined clay cement (LC3). Cement Concr Res 2019;115:70–9.
[91] Dang J, Du H, Pang SD. Hydration, strength and microstructure evaluation of eco-friendly mortar containing waste marine clay. J Clean Prod 2020;272:122784.
[92] Maraghechi H, Avet F, Wong H, Kamyab H, Scriwener K. Performance of Limestone Calcined Clay Cement (LC3) with

various kaolinite contents with respect to chloride transport. Mater Struct 2018;125:1251–7.
[93] Toutanji H, McNeil S, Bayasi Z. Chloride permeability and impact resistance of polypropylene-fiber-reinforced silica fume concrete. Cement Concr Res 1998;28(7):961–8.
[94] Toutanji HA. Properties of polypropylene fiber reinforced silica fume expansive-cement concrete. Construct Build Mater 1999;13:171–7.
[95] Zhang Mao-hua, Li Hui. Pore structure and chloride permeability of concrete containing nano-particles for pavement. Construct Build Mater 2011;25(2):608–16.
[96] Ben Haha M, De Weerdt K, Lothenbach B. Quantification of the degree of reaction of fly ash. Cement Concr Res 2010;40:1620–9.
[97] Dhandapani Y, Santhanam M. Assessment of pore structure evolution in the limestone calcined clay cementitious system and its implications for performance. Cement Concr Compos 2017;84:36–47.
[98] Ferreiro S, Herfort D, Damtoft J. Effect of raw clay type, fineness, water-to-cement ratio and fly ash addition on workability and strength performance of calcined clay–limestone Portland cements. Cement Concr Res 2017;101:1–12.
[99] Şahmaran MS, ̇Ozbay E, Yücel HE, Lachemi M, Li VC. Effect of fly ash and PVA fiber on microstructural damage and residual properties of engineered cementitious composites exposed to high temperatures. J Mater Civ Eng 2011;23(12):1735–45.
[100] Zhang D, Shao Y. Surface scaling of CO2-cured concrete exposed to freeze-thaw cycles. J CO2 Util 2018;27:137–44.
[101] Wu ZW, Lian HZ. High performance concrete. Beijing: Railway Press of China; 1999. p. 43 [in Chinese].
[102] Mehta PJM, Kumar P. Monteriro, concrete microstructure, properties, and materials. 2006.